

# ABSTRACT

JEFFREY KEITH JEPSON. Enhancements to the Inverse Design of Low-Speed Natural-Laminar-Flow Airfoils. (Under the direction of Dr. Ashok Gopalarathnam.)

The objective of inverse airfoil design has traditionally been the determination of the airfoil shape that results in desired aerodynamic characteristics. Under this general classification, inverse methods have progressed a great deal over the past few decades. With modern inverse methods, it is possible to prescribe velocity and/or boundary-layer characteristics along with desired geometric constraints in the design of airfoils. In spite of these advances, inverse airfoil design still involves a certain amount of trial and error when a designer attempts to fine tune the drag polar of the airfoil or when attempting to tailor the airfoil for a particular application. The research presented in this thesis makes two specific advances to the state of the art in inverse design. The first part of the research describes the development of an approach by which a desired boundary-layer transition curve can be specified as an input to inverse design. The second part presents an approach for incorporating aircraft performance considerations in the inverse design process. The two advances can help reduce the design cycle time for airfoil and aircraft design by reducing the amount of trial and error in the design process.

The motivation factor for the first part of the research (inverse design via specification of the boundary-layer transition curve) was the strong connection between the transition curve and the airfoil drag polar. In the approach developed, a multidimensional Newton iteration is used to adjust the velocity distribution until the transition lift coefficient at several locations on the airfoil are within a given tolerance of the specifications. It is shown that the shape of the drag bucket as well as the camber and extents of laminar flow on the airfoil can be controlled through the specification of the transition-curve. This method represents an enhancement over previous inverse airfoil design methods since it allows for a single specification that spans multiple operating points.

The second part of the research (incorporation of aircraft performance considerations in inverse airfoil design) was driven by a motivation to incorporate airfoil-aircraft matching considerations in the airfoil design process. Two aircraft

performance parameters are considered in this work: level-flight maximum speed and maximum range. Through the use of a multidimensional Newton iteration, the method adjusts the lift coefficients for the corners of the low-drag region of the drag polar to tailor the airfoil for the two flight conditions. The results from the design method are validated using a post-design aircraft performance simulation. This method results in the next level of sophistication in inverse airfoil design technology since system-level performance considerations are used to drive the airfoil design.

# Enhancements to the Inverse Design of Low-Speed Natural-Laminar-Flow Airfoils

by

**Jeffrey Keith Jepson**

A thesis submitted to the Graduate Faculty of  
North Carolina State University  
in partial fulfillment of the  
requirements for the Degree of  
Master of Science

**Aerospace Engineering**

Raleigh, NC  
2003

**APPROVED BY:**

---

Dr. Ashok Gopalarathnam  
Advisory Committee Chairman

---

Dr. James F. Selgrade  
Advisory Committee Minor Rep.

---

Dr. Jack R. Edwards  
Advisory Committee Member

To Mom, Dad, and Angela

Without your love and support I would not be where I am today.

## BIOGRAPHY

Jeffrey Keith Jepson was born on August 11, 1979 in Brooksville, FL to James and Laraine Jepson. He attended Sanderson High School in Raleigh, NC where he played alto saxophone in the marching band. He graduated in 1997 and started college at North Carolina State University. He graduated summa cum laude with a BS in Aerospace Engineering in May 2001.

He joined the applied aerodynamics group at North Carolina State University in the fall of 2001 as a graduate research assistant for Dr. Ashok Gopalarathnam. Under the guidance of Dr. Gopalarathnam, Jeffrey worked on many research projects in the areas of airfoil design and design methodologies, resulting in two AIAA conference papers and a forum at the 2003 EAA Airventure. After graduation, Jeffrey plans to continue his work under Dr. Gopalarathnam in the area of adaptive aerodynamics towards a PhD in Aerospace Engineering.

## ACKNOWLEDGEMENTS

First and foremost I would like to thank my advisor, Dr. Ashok Gopalarathnam. This work would not be possible without his support and dedication as well as the belief in my potential as a graduate student.

I would also like to thank Dr. James F. Selgrade and Dr. Jack R. Edwards for agreeing to be on my committee. I had the privilege of taking classes from both of them. I greatly enjoyed the classes and learned a lot from them.

In addition, I would like to thank the many graduate students and faculty that I have known over the past two years. In one way or another, you all have helped me with this work.

I would also like to thank Angela for being who you are and for putting up with me through the good times and the bad times. I couldn't have done this without you.

Finally, I would like to thank my parents for giving me the tools I need to achieve my goals. Without your love, support, and guidance this work would not be possible.

# Table of Contents

<b>List of Tables</b> . . . . .	<b>viii</b>
<b>List of Figures</b> . . . . .	<b>ix</b>
<b>Nomenclature</b> . . . . .	<b>xi</b>
<b>Chapter 1 Introduction</b> . . . . .	<b>1</b>
1.1 Background . . . . .	1
1.2 Research Objectives . . . . .	6
1.3 Outline of Thesis . . . . .	8
<b>Chapter 2 Boundary-Layer Transition Specification in Inverse Airfoil Design</b> . . . . .	<b>10</b>
2.1 Methodology for Transition-Curve Specification . . . . .	11
2.1.1 Brief Description of the PROFOIL Code . . . . .	11
2.1.2 Overview of the Transition-Specification Approach . . . . .	13
2.1.3 Detailed Formulation of Transition Specification . . . . .	15
2.2 Demonstration of Transition-Specification Capability . . . . .	17
2.2.1 Single Specification for an NLF Airfoil with Validation . . . . .	18
2.2.2 Family of NLF Airfoils with Varying Transition Curve Slopes . . . . .	20
2.2.3 Family of NLF Airfoils with Various Amounts of Camber . . . . .	22
2.2.4 Family of NLF Airfoils with Various Extents of Laminar Flow . . . . .	25

2.3	Summary . . . . .	27
<b>Chapter 3</b>	<b>Aircraft Performance Considerations in Inverse Airfoil Design . . . . .</b>	<b>29</b>
3.1	Methodology . . . . .	30
3.1.1	Overview of the Design Formulation . . . . .	30
3.1.2	Illustration of the Approach . . . . .	31
3.1.3	Airfoil Tailoring for $V_{max}$ . . . . .	35
3.1.4	Airfoil Tailoring for $R_{max}$ . . . . .	36
3.2	Analysis Tools for Validation . . . . .	39
3.3	Aircraft Specifications . . . . .	40
3.4	Demonstration . . . . .	41
3.4.1	Airfoil Tailoring for $V_{max}$ . . . . .	43
3.4.2	Airfoil Tailoring for $R_{max}$ . . . . .	45
3.4.3	Airfoil Tailoring for $V_{max}$ and $R_{max}$ . . . . .	48
3.5	Discussion of Results . . . . .	54
<b>Chapter 4</b>	<b>Concluding Remarks . . . . .</b>	<b>55</b>
4.1	Summary of Research . . . . .	55
4.1.1	Boundary-Layer Transition Curve Specification . . . . .	55
4.1.2	Incorporation of Aircraft Performance Considerations . . . . .	56
4.2	Future Work . . . . .	58
4.2.1	Incorporation of Constant-Landing-Speed Option . . . . .	58
4.2.2	Extension of the Approaches for Adaptive Airfoils . . . . .	59
<b>Chapter 5</b>	<b>References . . . . .</b>	<b>61</b>
<b>Appendix A</b>	<b>Brent's Method for Root Finding . . . . .</b>	<b>65</b>

Appendix B	Skin-Friction Drag Estimate . . . . .	67
------------	---------------------------------------	----

# List of Tables

3.1 Assumed geometry, drag, and power characteristics for the hypothetical general aviation airplane. . . . . 42

# List of Figures

1.1	Flowchart of Direct Design. . . . .	2
1.2	Flowchart of Inverse Design Based on Velocity Distribution. . . . .	3
1.3	Flowchart of Airfoil/Aircraft Matching. . . . .	6
1.4	Flowchart of Inverse Design Based on Transition Specification . . . . .	7
1.5	Flowchart of Inverse Design with Aircraft Performance Considerations . . . . .	8
2.1	Geometry and velocity distribution for three NLF airfoils with systematic variations in the lower-surface velocity distribution. . . . .	14
2.2	Changes to the lower-surface transition curve from XFOIL analysis for $Re$ of 4 million. . . . .	14
2.3	Transition specification points on a segment of the lower surface of the airfoil . . . . .	16
2.4	Velocity spline support and specification points . . . . .	16
2.5	Initial and converged lower-surface transition curves calculated using PROFOIL. . . . .	18
2.6	Inviscid velocity distributions for initial and converged airfoils. . . . .	19
2.7	Performance of initial and converged airfoils predicted using XFOIL. . . . .	19
2.8	Converged lower-surface transition curves for airfoils $D$ , $E$ , and $F$ calculated using PROFOIL. . . . .	21
2.9	Inviscid velocity distributions for airfoils $D$ , $F$ , and $F$ . . . . .	21
2.10	Performance of airfoils $D$ , $E$ , and $F$ predicted using XFOIL. . . . .	22
2.11	Converged lower-surface transition curves for airfoils $G$ , $H$ , and $I$ calculated using PROFOIL. . . . .	23
2.12	Inviscid velocity distributions for airfoils $G$ , $H$ , and $I$ . . . . .	24
2.13	Performance of airfoils $G$ , $H$ , and $I$ predicted using XFOIL. . . . .	24
2.14	Converged lower-surface transition curves for airfoils $J$ , $K$ , and $L$ calculated using PROFOIL. . . . .	26
2.15	Inviscid velocity distributions for airfoils $J$ , $K$ , and $L$ . . . . .	26
2.16	Performance of airfoils $G$ , $H$ , and $I$ predicted using XFOIL. . . . .	27
3.1	Airfoil drag polar used for illustration. . . . .	31
3.2	Drag polars for the baseline airfoil and the airfoil tailored for $V_{max}$ . . . . .	33
3.3	Illustration of the effect of the lower corner of LDR on $V_{max}$ . . . . .	33
3.4	Drag polars for the baseline airfoil and the airfoil tailored for $R_{max}$ . . . . .	34

3.5	Illustration of the effect of the upper corner of LDR on $R_{max}$ . . .	34
3.6	Comparison between flat plate drag and total drag at $Re\sqrt{C_l} = 3.42 \times 10^6$ . . . . .	37
3.7	Flowchart of $V_{max}$ tailoring routine. . . . .	37
3.8	Flowchart of $R_{max}$ tailoring routine. . . . .	39
3.9	Planview showing the right-side geometry of the wing and tail for hypothetical aircraft. . . . .	41
3.10	Assumed propeller efficiency distribution. . . . .	42
3.11	Geometries and inviscid velocity distributions for the baseline airfoil and the converged airfoil M. . . . .	43
3.12	Polars for the baseline airfoil and the converged airfoil M from XFOIL analysis. . . . .	44
3.13	Rate of climb curves for the baseline airfoil and the converged airfoil M. . . . .	44
3.14	Drag polars for airfoils M, M1, and M5 . . . . .	46
3.15	$V_{max}$ as a function of $C_l^{low}$ . . . . .	46
3.16	Rate of climb curves for airfoils M, M1, and M5 . . . . .	47
3.17	Geometries and inviscid velocity distributions for the baseline airfoil and the converged airfoil N. . . . .	48
3.18	Polars for the baseline airfoil and the converged airfoil N from XFOIL analysis. . . . .	49
3.19	Range curves for the baseline airfoil and the converged airfoil N. . . . .	49
3.20	Drag polars for airfoils N, N1, and N5 . . . . .	50
3.21	Maximum range as a function of $C_l^{up}$ . . . . .	50
3.22	Rate of climb curves for airfoils N, N1, and N5 . . . . .	51
3.23	Geometries and inviscid velocity distributions for the baseline airfoil and the converged airfoil O. . . . .	52
3.24	Polars for the baseline airfoil and the converged airfoil O from XFOIL analysis. . . . .	52
3.25	Rate of climb curves for the Baseline airfoil and the converged airfoil O. . . . .	53
3.26	Range curves for the Baseline airfoil and the converged airfoil O. . . . .	53
4.1	Lift curves for the Baseline airfoil and airfoil M . . . . .	58
4.2	Drag polars for NASA NLF(1)-0215F airfoil with various flap deflections from XFOIL analysis . . . . .	60
B.1	Flat Plate Boundary-Layer Approximation . . . . .	68

# Nomenclature

$AR$  wing aspect ratio

$b$  wing span

$c$  chord length

$C_D$  aircraft or wing drag coefficient based on  $S_w$

$C_d$  airfoil drag coefficient based on the chord

$C_L$  aircraft or wing lift coefficient based on  $S_w$

$C_l$  airfoil lift coefficient based on the chord

$C_m$  airfoil pitching moment coefficient about the quarter-chord location

$H_{12}$  shape factor

$LDR$  low-drag region

$M$  Mach number

$n$  transition amplification factor

$NLF$  natural laminar flow

$P_{av}$  power available

$P_{req}$  power required

$R$	aircraft range
$ROC$	aircraft rate of climb
$Re$	Reynolds number
$S$	area
$sfc$	specific fuel consumption
$V$	aircraft velocity
$W$	aircraft weight
$W_e$	aircraft weight without fuel
$W_f$	aircraft weight with fuel
$X_t$	length of laminar boundary-layer
$x_{tr}$	transition location
$X_{Tt}$	length of hypothetical turbulent boundary-layer
$\alpha$	angle of attack
$\eta_p$	propeller efficiency
$\rho$	density

### **Subscripts**

$0l$	zero lift
$c.g.$	center of gravity
$crit$	critical value

*desired* desired value

*f* fuselage and other components of aircraft except wing

*i* induced

*max* maximum

*min* minimum

*p* profile

*trans* transition value

*w* wing

### **Superscripts**

*low* lower corner of the airfoil low-drag range

\*

design value

*up* upper corner of the airfoil low-drag range

# Chapter 1

## Introduction

### 1.1 Background

Airfoil design methods can be broadly classified into two types: direct and inverse. In a direct method, the airfoil shape is used as the starting point for the design cycle. The resulting aerodynamics are then computed as an output of the design. By successively adjusting the shape, the design approach works towards obtaining an airfoil that results in the desired performance. Figure 1.1 shows a schematic representation of this process, in which the airfoil shape is used to compute the velocity distributions, boundary-layer characteristics, the laminar-to-turbulent transition location and finally the drag polar. This and the subsequent flowcharts were adapted from the ones developed by Michael Selig. While many successful airfoils have been designed using direct design methods, most notably the NACA four-digit airfoils, a large amount of trial and error is involved in obtaining an airfoil with the desired performance.

In contrast, the objective of an inverse airfoil design method is to determine the shape of the airfoil that satisfies desired aerodynamic and geometric specifications. The first pioneering methods (such as those by Mangler<sup>1</sup> and by Lighthill<sup>2</sup>) allowed for the prescription of the desired inviscid velocity distribution at a single angle of attack. Figure 1.2 provides an outline of these early methods. The

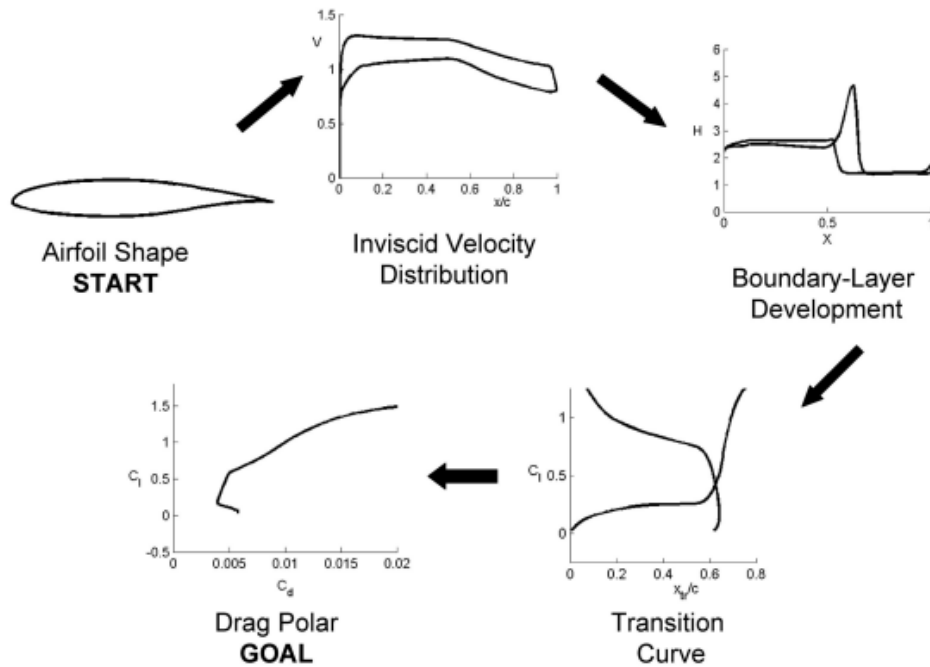


Figure 1.1: Flowchart of Direct Design.

motivation behind these methods was to take advantage of the relationship between the velocity distribution and other aerodynamic properties such as lift, drag, and pitching moment. These relationships result from the fact that velocity is a measure of surface pressure. Therefore, the airfoil lift at any angle of attack is essentially the area between the velocity curves for the upper and lower surfaces. In addition, the pitching moment is determined from the chordwise distribution of this area. The velocity gradients over the airfoil also determine the boundary layer development. From the boundary layer development, the drag can be determined. Therefore, the overall performance of the airfoil can be indirectly controlled by specifying the velocity distribution.

Subsequently, to enable more direct control over the final airfoil performance, inverse airfoil design methods were developed that allowed for boundary-layer development specifications (e.g. Henderson<sup>3</sup>). In these methods, an inverse

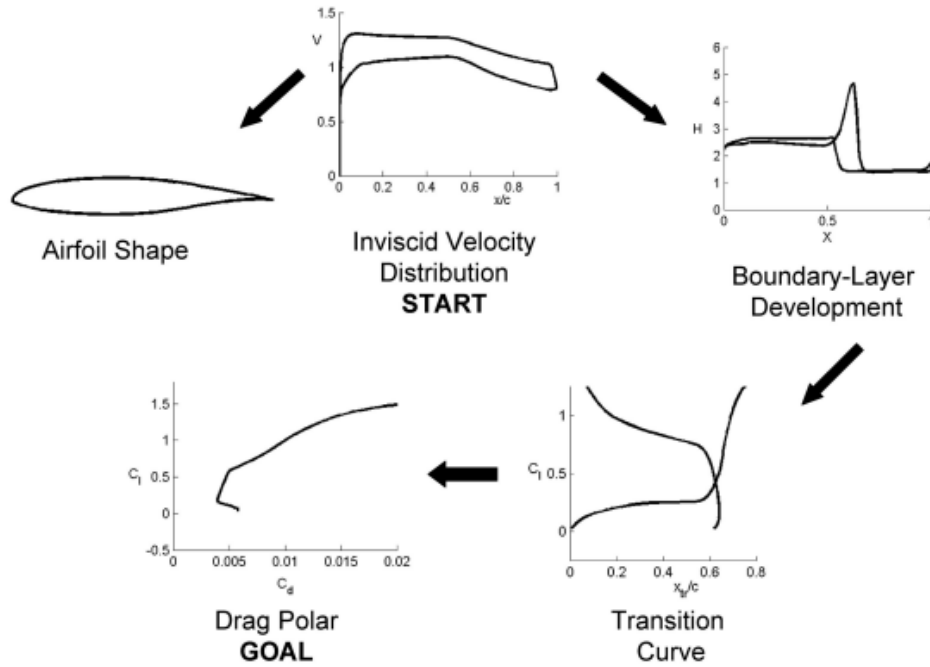


Figure 1.2: Flowchart of Inverse Design Based on Velocity Distribution.

boundary-layer method is first used to determine the velocity distribution that results in a desired boundary-layer development. This velocity distribution is then used to determine the airfoil shape. While these methods significantly improved the capability to design airfoils, they were all single-point methods. That is, with these methods, the desired velocity and/or boundary-layer properties can be specified at only one operating point (airfoil  $C_l$  and  $Re$ ) and the performance at off-design conditions has to be determined via post-design analysis. Since airfoils need to operate at multiple conditions for most applications, there was a need for multipoint inverse design approaches.

One of the first practical multipoint inverse approaches was developed by Eppler in 1957.<sup>4-6</sup> The approach has been used for the design of numerous airfoils.<sup>6-9</sup> In Eppler's conformal mapping-based inverse method, the airfoil is divided into several segments and over each segment the design angle of attack,  $\alpha^*$ , (measured

relative to the zero-lift angle of attack) is prescribed. The method then determines the airfoil shape such that the velocity gradient over a given segment is zero when operating at the  $\alpha^*$  of that segment. Since the velocity gradients become progressive more adverse on the upper surface with increase in airfoil  $\alpha$  and vice versa on the lower surface, specifying the  $\alpha^*$  for a segment is an indirect means of specifying the velocity distribution over that segment. This approach allows for multipoint design since each segment can have a unique  $\alpha^*$ , thus enabling control of the velocity distribution over different portions of the airfoil at different values of  $C_l$ .

The basic theory of Eppler was used by Selig and Maughmer<sup>10,11</sup> to develop the PROFOIL design code, which significantly extends the inverse airfoil design capability of Eppler's method. Two major advances over the Eppler code are (i) the coupling of a direct integral boundary-layer method with the potential-flow inverse airfoil design theory and (ii) the development of a multidimensional Newton iteration capability that allows for the simultaneous specification of desired velocity, boundary-layer and geometric specifications in the design of the airfoil. In order to achieve these specifications, the Newton iteration scheme is used to automatically adjust user-selected input variables in the initial definition of the airfoil. In the recent past, the Newton iteration capability in PROFOIL has been further expanded in a hybrid approach to couple the inverse design method with two- and three-dimensional panel codes<sup>12,13</sup> in order to allow for the design of complex configurations such as multi-element airfoils<sup>14,15</sup> and airfoil sections for wings and junctures.<sup>15,16</sup> Thus the PROFOIL code has powerful multipoint design capabilities that are useful in a variety of aerodynamic design scenarios.

Recent work by Gopalarathnam and Selig<sup>17</sup> and Jepson and Gopalarathnam<sup>18</sup> illustrate the power of inverse approaches in the design of low-speed natural laminar flow (NLF) airfoils by showing how it is possible to reliably control the  $C_l$

values of the upper and lower corners of the low-drag range (LDR or drag bucket) by appropriate specification of the velocity and boundary-layer properties on different segments of the airfoil along with the design lift coefficients and Reynolds numbers for the segments. By altering the chordwise locations and extents of these segments, it is possible to adjust the extents of the favorable pressure gradients on the upper and lower surfaces of the airfoil, thus controlling the extents of laminar flow and the resulting  $C_d$  at the design conditions. With these capabilities, modern inverse methods allow for easy generation of families of airfoils with systematic changes in the lift, drag, and pitching moment characteristics.

While inverse design methods have made it relatively easy to design families of airfoils with desired aerodynamics, there is still the matter of selecting the proper airfoil for a given application. The process of tailoring an airfoil for an end application (such as a given aircraft) typically involves cycling through airfoil design and aircraft performance simulations—a trial-and-error process. The results of such aircraft performance simulations enable the examination of the trade-offs involved in the choices of the different airfoil design parameters such as the  $C_l$  values for the upper and lower corners of the LDR. Figure 1.3 shows an outline of a typical airfoil-aircraft matching process. In the method, the airfoil is designed using a desired velocity distribution as an input and the resulting aircraft configuration is then analyzed. If the aircraft performance does not match the desired specifications, the airfoil velocity distribution is changed and this process continues until the desired aircraft performance is achieved.

Surprisingly little work has been done to improve airfoil-aircraft matching. However, the airfoil selection process can be made considerably easier by the use of a figure-of-merit approach<sup>19</sup> for airfoil-aircraft design integration or by the use of closed-form analytical expressions for the ideal  $C_l$  values for the LDR upper and lower corners such as those derived by Gopalarathnam and McAvoy<sup>20</sup> for

piston-propeller powered aircraft with constant values of the propeller efficiency and engine specific fuel consumption. In spite of these improvements, the process of the tailoring of airfoils for an aircraft still relies on numerous post-design aircraft performance simulations.

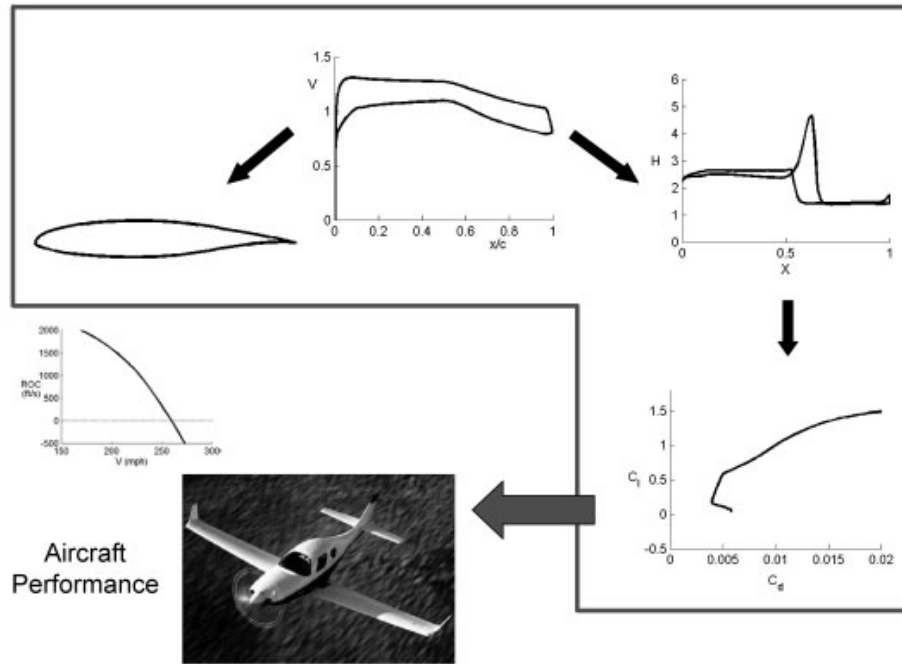


Figure 1.3: Flowchart of Airfoil/Aircraft Matching.

## 1.2 Research Objectives

The overall objective of the research was to improve the state of the art in inverse airfoil design. The focus of the first part of the research was to develop an inverse approach that allowed for the specification of the boundary-layer transition curves as an input to the design method. This was done by extending the inverse design capability in PROFOIL to allow for the specification of a desired transition curve over multiple segments of an airfoil. Transition curve, in this work, refers to

the plot of airfoil  $C_l$  vs.  $x_{tr}/c$  for the upper or lower surface of that airfoil at a specified  $Re$ , as shown in Fig. 1.4. The overall scheme of this method is presented in Fig. 1.4. It can be seen that the transition curve is used as the starting point of the design process. The motivation for specifying the transition curve arises from the fact that in several design situations, there is a strong connection between the shape of the transition curve and the airfoil performance.<sup>17,21</sup>

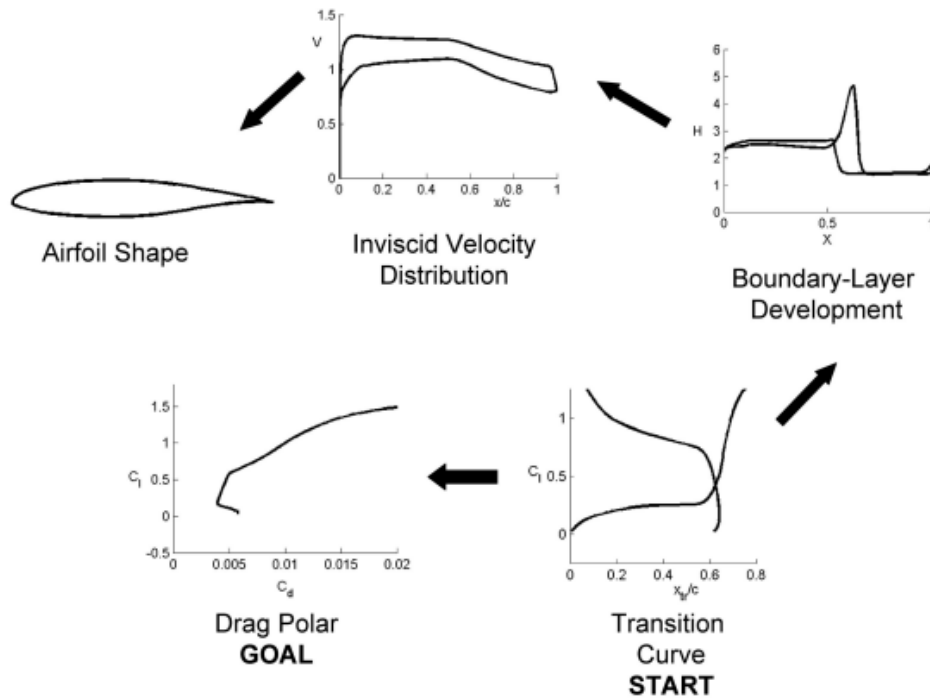


Figure 1.4: Flowchart of Inverse Design Based on Transition Specification

The second part of the research focused on the development of an approach that allows for the specification of aircraft performance considerations as inputs to inverse airfoil design. The two aircraft performance parameters considered in this work are aircraft level-flight maximum speed and maximum range. Figure 1.5 shows an outline of the approach in which aircraft performance is used as a starting point for the inverse design. Such an advancement results in the next level of sophistication in inverse airfoil design technology, as a result of which the inputs

to the inverse design can be expanded beyond the desired airfoil aerodynamics to include the characteristics of the intended aircraft such as wing area, wing span, fuselage drag, and engine power. Overall design cycle time can also be considerably reduced by using such a method.

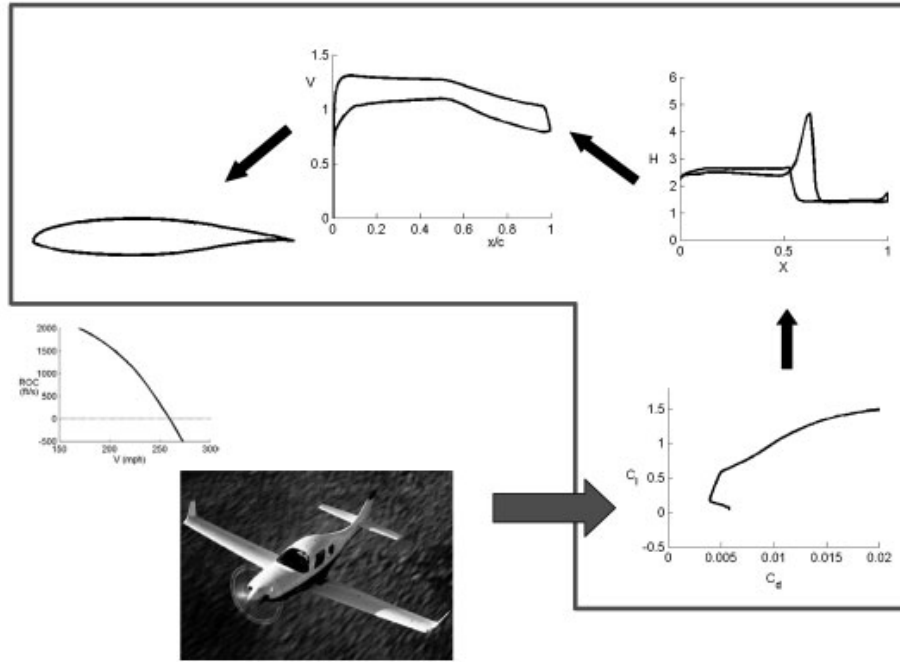


Figure 1.5: Flowchart of Inverse Design with Aircraft Performance Considerations

### 1.3 Outline of Thesis

Chapter 2 presents the inverse airfoil design approach that allows for the use of the boundary-layer transition curve as an input. The chapter starts with the methodology used to develop the method. A brief description of the PROFOIL code is first presented. This is followed by an outline of the transition-specification approach. The detailed formulation of the transition is then presented. The rest of the chapter presents several examples that demonstrate the usefulness of

the method. The incorporation of aircraft performance considerations in inverse design is presented in Chapter 3. An overview of the design formulation is first presented. A detailed description of the formulation used to tailor the airfoil for level-flight maximum speed,  $V_{max}$ , and maximum range,  $R_{max}$ , is then shown. This is followed by a description of the analysis tools used for validation of the results from the design method. Finally, examples are presented to illustrate the capabilities of the method. Lastly, Chapter 4 presents some conclusions as well as some future work that will be performed in this area.

## Chapter 2

# Boundary-Layer Transition Specification in Inverse Airfoil Design

The main objective of the first portion of the research that is presented in this chapter was to develop an inverse airfoil design method that uses boundary-layer transition curve specifications as inputs in order to take advantage of the strong connection between the shape of the transition curve and the overall airfoil performance. Three examples of airfoil design situations are listed here to illustrate this strong connection. (1) On low-speed natural-laminar-flow (NLF) airfoils, the rate at which the lower-surface transition location moves forward with decrease in  $\alpha$  determines the sharpness of the lower corner of the drag bucket. That is, the slope of the transition curve can be used to control the shape of the lower corner of the drag bucket.<sup>17</sup> (2) The sensitivity of the airfoil  $C_{lmax}$  to roughness can be minimized by using an upper-surface transition location that moves forward gradually with increasing  $\alpha$  such that transition occurs at the leading edge at  $C_{lmax}$ .<sup>22</sup> (3) The shape of the drag polar for low Reynolds number airfoils is closely dependent on the shape of the transition curve. A steeper transition curve is associated with higher bubble drag and vice versa.<sup>6,21,23</sup>

Because of this strong correlation between the transition curve and the final

performance of the airfoil, it is worthwhile searching for a method that allows for the specification of the transition curve in the inverse airfoil design process. The following section presents the methodology used to enhance the capabilities of PROFOIL to include such specifications. Examples are then presented in the next section to demonstrate the usefulness of the method.

## 2.1 Methodology for Transition-Curve Specification

In order to achieve inverse design through transition-curve specification, the inverse airfoil design method PROFOIL<sup>10,11</sup> was enhanced. This section first briefly describes some of the main features of the PROFOIL code. An overview of the current approach used to incorporate the transition-curve specification is presented next. The details of the formulation are then described.

### 2.1.1 Brief Description of the PROFOIL Code

PROFOIL<sup>10,11</sup> is a multipoint inverse design method based on conformal mapping. In the method, the airfoil is divided into a finite number of segments each having a design angle of attack,  $\alpha^*$ , that is measured relative to  $\alpha_{0l}$ . At each segment  $\alpha^*$ , the velocity distribution over the segment is prescribed and can either be a constant (as in the Eppler method) or can have a nonlinear variation using a cubic spline description.<sup>11</sup> Specifying  $\alpha^*$  is equivalent to specifying a design value of  $C_l$ , referred to as  $C_l^*$ , since  $\alpha^*$  is measured from the zero-lift line and the slope of the lift curve is approximately  $2\pi$  per radian. In other words, the design lift coefficient for any segment is related to the segment  $\alpha^*$  (in degrees) by Eq. 2.1.

$$C_l^* \approx 0.1 \times \alpha^* \quad (2.1)$$

PROFOIL can also solve for the boundary layer development along the upper and lower surfaces of the airfoil at a specified  $C_l$  using a direct integral method. For a given airfoil, PROFOIL uses the inviscid velocity distribution to calculate boundary-layer properties such as the shape factor  $H_{12}$  and the development of the transition amplification factor  $n$ . Since this boundary-layer calculation is used in conjunction with the rapid, interactive design environment in PROFOIL, no viscous-inviscid interaction (VII) is used. In other words, the inviscid pressure distribution is not adjusted due to the effects of the boundary-layer displacement thickness. The  $n$  development is calculated using Drela's approximate  $e^n$  method.<sup>24,25</sup> In the current work, transition is assumed to occur when  $n$  reaches a specified critical value,  $n_{crit}$ . This assumption is valid for flows where transition is caused by the amplification of Tollmien-Schlichting waves.

One of the main features of PROFOIL is the multidimensional Newton iteration scheme that allows for the prescription of several aerodynamic and geometric characteristics. This multidimensional Newton iteration scheme is utilized as a key element in the current work to allow for the various specifications discussed later. In this scheme, control over some of the parameters used in conformal mapping is given up in order to achieve the desired specifications. These parameters are altered through the Newton iteration until the desired specifications are satisfied. The goal of the Newton iteration is to solve the following matrix equation (Eq. 2.2).

$$\mathbf{J} \cdot \delta \mathbf{x} = -\mathbf{F} \quad (2.2)$$

In this matrix equation,  $\mathbf{F}$  is the vector containing the residuals of the functions

to be zeroed,  $\mathbf{J}$  is the  $n \times n$  Jacobian matrix that contains the gradient information, and  $\delta\mathbf{x}$  contains the corrections to the design variables to make  $\mathbf{F}$  approach zero. For each iteration,  $\delta\mathbf{x}$  is found and applied to the design variables. This process continues until the desired specifications are achieved to within a given tolerance.

### 2.1.2 Overview of the Transition-Specification Approach

To illustrate the approach used in the current work for achieving a desired transition curve, a family of three NLF airfoils is considered with special focus on a segment on the lower surface. Figure 2.1 shows the geometries and velocity distributions for the NLF airfoils with three systematic variations in the velocity distribution for this lower-surface segment. The beginning and end points of this segment are marked in the plots. The design specifications for the three airfoils were all identical except for the velocity variation on the lower-surface segment. The maximum thickness ratio was specified to be 14% for the three airfoils.

Figure 2.2 shows the resulting lower-surface transition curves as predicted by the XFOIL code<sup>24</sup> for the three airfoils, with the  $x_{tr}/c$  locations for the beginning and end points of the lower-surface segment marked. It can be seen that the perturbations to the velocity distribution on a segment result in systematic but nonlinear changes to the transition curve. These results show that while the velocity distribution on a segment is the appropriate design variable for achieving a desired transition curve, achieving a desired transition curve by manually adjusting the velocity variation would be tedious. The problem, however, is ideally suited to being solved as a system of nonlinear equations in the Newton iteration scheme available in the PROFOIL. The details of this formulation are presented in the following subsection.

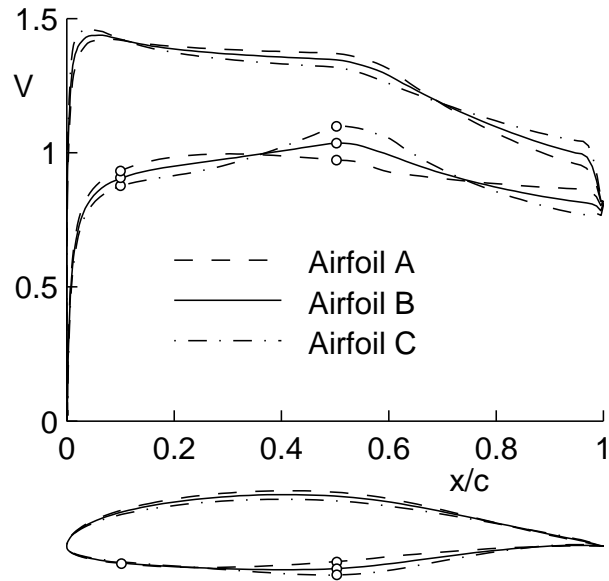


Figure 2.1: Geometry and velocity distribution for three NLF airfoils with systematic variations in the lower-surface velocity distribution.

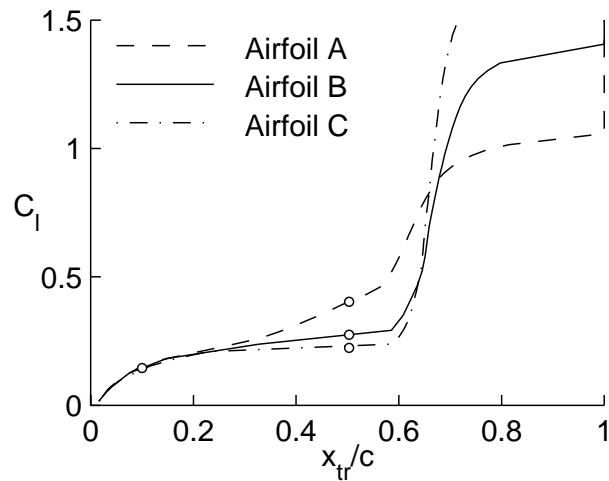


Figure 2.2: Changes to the lower-surface transition curve from XFOIL analysis for  $Re$  of 4 million.

### 2.1.3 Detailed Formulation of Transition Specification

In the current formulation, the desired shape of the transition curve is defined by identifying discrete locations on a segment and then determining desired value of the transition  $C_l$ ,  $C_{l_{trans,desired}}$ , at each of these locations, as illustrated in Fig. 2.3. The figure shows a segment of the lower-surface transition curve along with the specification points. While only three points are used in this illustration, any number of specification points are possible. The nonlinear velocity distribution over the segment, which is defined using spline support points, is then adjusted using the Newton iteration scheme in order to bring the  $C_{l_{trans}}$  to within a specified tolerance of the desired value  $C_{l_{trans,desired}}$  at each of the discrete points. These spline support points are shown in Fig. 2.4 along with the design-variable points for the segment. As can be seen, the design-variable points do not need to coincide with the spline support points. The residual for the Newton equation for any one of these discrete specification points can then be expressed as shown in Eq. 2.3. The element of the Jacobian that contains the sensitivity of the  $C_{l_{trans}}$  to changes in the velocity,  $v$ , at one of the spline support points can be expressed as shown in Eq. 2.4.

$$F = C_{l_{trans,desired}} - C_{l_{trans}} \quad (2.3)$$

$$J_{i,j} = \frac{\partial C_{l_{trans}}}{\partial v} \quad (2.4)$$

The method developed to determine the  $C_{l_{trans}}$  for a given location needs special mention. The transition location  $x_{tr}/c$  for any given  $\alpha$  or  $C_l$  is determined using the direct integral boundary-layer method by calculating the location at which the value of the transition amplification factor  $n$  equals the user-specified critical value of  $n_{crit}$ . Determination of the  $C_{l_{trans}}$  for a given  $x/c$ , on the other

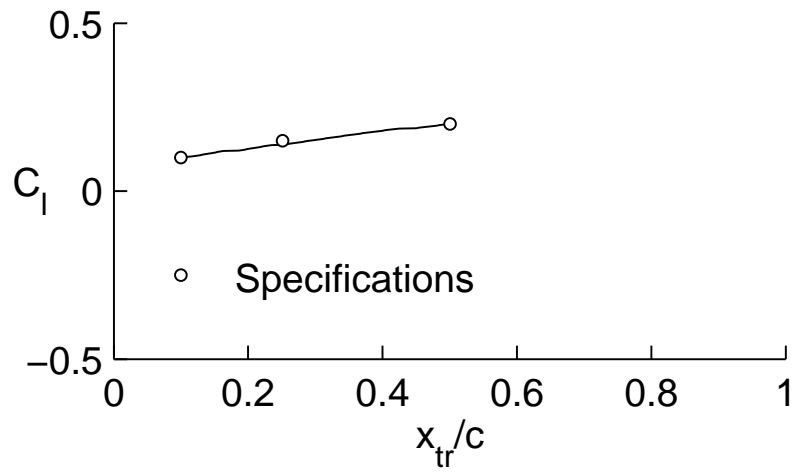


Figure 2.3: Transition specification points on a segment of the lower surface of the airfoil

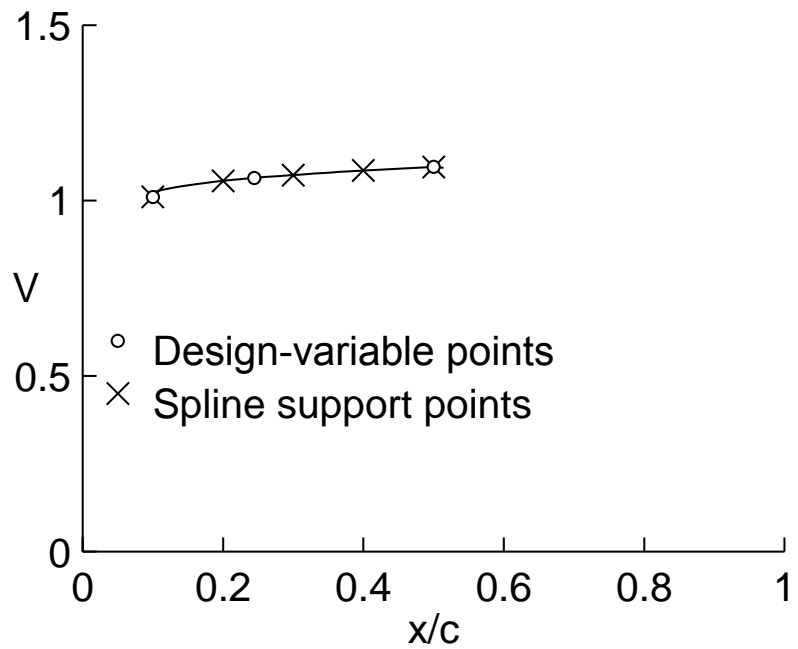


Figure 2.4: Velocity spline support and specification points

hand, requires iteration on the  $C_l$  with an integral boundary-layer computation for each iteration. Because this iteration may potentially need to be performed several hundred times in the Newton scheme, an efficient method for computing the  $C_{ltrans}$  was needed.

The current work uses a one-dimensional root-finding method known as Brent's method<sup>26</sup> to determine  $C_{ltrans}$  at a given location. This method uses bisection, inverse quadratic interpolation and root bracketing to find the value of  $C_{ltrans}$  at a given location. A detailed description of Brent's Method can be found in Appendix A. Using Brent's method to calculate  $C_{ltrans}$  provides a relatively quick and reliable way of determining the transition location both for computing the residual as well as for the effect of a perturbation during the calculation of the Jacobian.

These Newton equations for achieving specified values for the  $C_{ltrans}$  at the discrete points on the design segment were integrated into the existing Newton iteration procedure in PROFOIL. These enhancements to the PROFOIL code enable achieving a desired transition-curve shape at one or more segments while simultaneously satisfying additional specifications on velocity, boundary-layer parameters, and geometry parameters such as airfoil thickness ratio. The following section presents examples to demonstrate the capability of the current method.

## 2.2 Demonstration of Transition-Specification Capability

The inverse design capability is demonstrated in this section using four examples. In these examples, the design and analysis was performed at a constant  $Re\sqrt{C_l}$  of  $2.0 \times 10^6$ . Use of a constant  $Re\sqrt{C_l}$  takes into account the changes in  $Re$  as a result of changes in airspeed associated with variations in the operating  $C_l$ .

## 2.2.1 Single Specification for an NLF Airfoil with Validation

In the first example, an NLF airfoil is used as the initial starting point, and specifications are made to define the desired shape of the lower-surface transition curve at three discrete points. Figure 2.5 shows the initial and converged lower-surface transition curves using the integral boundary-layer in the PROFOIL code along with the design specifications. It is seen that the method successfully satisfies the prescriptions. The initial and final airfoil geometries and velocity distributions are shown in Fig. 2.6. It can be seen that the camber of the airfoil decreases due to the specification.

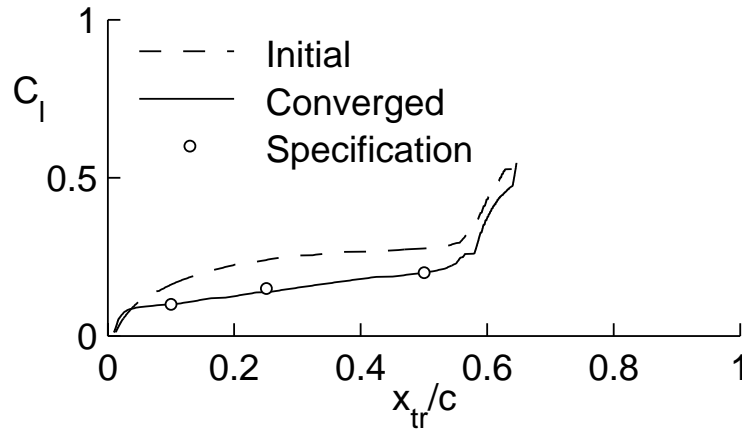


Figure 2.5: Initial and converged lower-surface transition curves calculated using PROFOIL.

In order to study the effect of the transition-curve specification on the airfoil performance, the initial and converged airfoils were analyzed using XFOIL. Figure 2.7 shows the plots comparing the drag polars, lift and moment curves, and the transition curves as predicted by XFOIL. Also shown as markers are the design transition specifications made at the three locations on the lower surface. It is seen that the transition curve from XFOIL analysis for the converged airfoil does not go through the specifications. The reason for this behavior is that

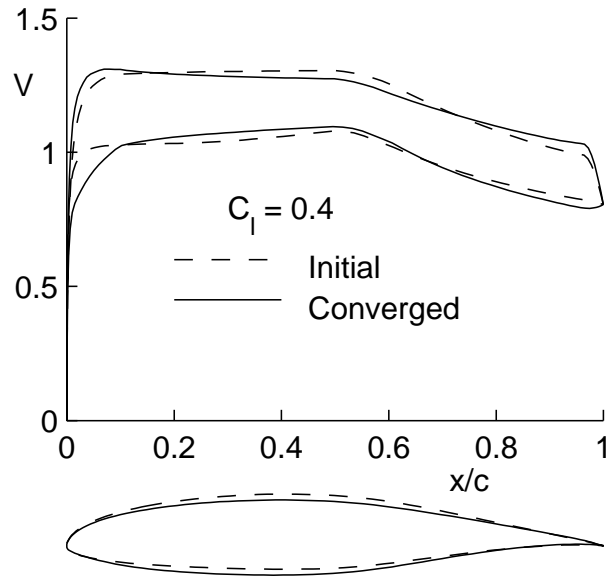


Figure 2.6: Inviscid velocity distributions for initial and converged airfoils.

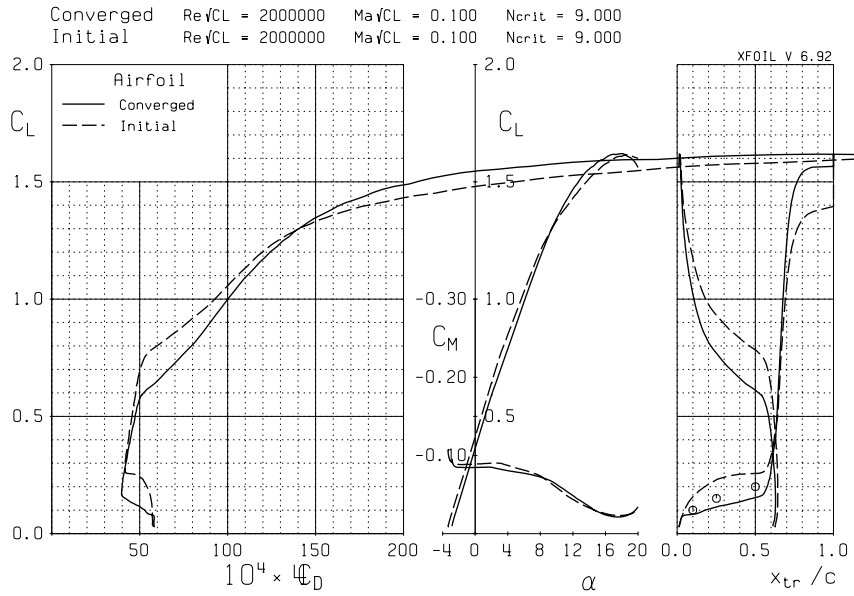


Figure 2.7: Performance of initial and converged airfoils predicted using XFOIL.

no VII effects are taken into account for the boundary-layer calculations in the PROFOIL design code, whereas VII effects are taken into account in the XFOIL analysis. Even though the transition curve for the converged airfoil shape from XFOIL analysis does not exactly satisfy the specifications, the trends between the initial and the converged airfoils from XFOIL closely match those specified in PROFOIL. The current method, therefore, can be used to reliably alter the transition curve even though the PROFOIL code does not consider VII effects.

### **2.2.2 Family of NLF Airfoils with Varying Transition Curve Slopes**

In the second example, a family of three NLF airfoils ( $D$ ,  $E$ , and  $F$ ) is considered. The airfoils were designed by specifying a different slope for the lower-surface transition curve for each of the airfoils, while maintaining the same extent of laminar flow on the lower-surface of the airfoil. The transition curve specifications as well as the converged lower-surface transition curves computed using PROFOIL for the three airfoils are presented in Fig 2.8. As the figure shows, the slope of the lower surface transition curve gradually increases from airfoil D to airfoil F. The airfoil geometries and velocity distributions for the three airfoils are shown in Fig. 2.9. It can be seen that the transition-curve specifications in this example do not have a significant effect on the shape of the airfoils.

XFOIL was again used to study the effects of the specifications on the aerodynamics of the airfoils. The resulting performance plots are shown in Fig. 2.10. As the figure shows, by keeping the amount of laminar flow constant and decreasing the slope of the transition curve, the lower corner of the drag bucket becomes more pronounced. This increases the performance of the airfoil at low speeds by increasing the performance at the upper corner of the drag bucket. It is seen that

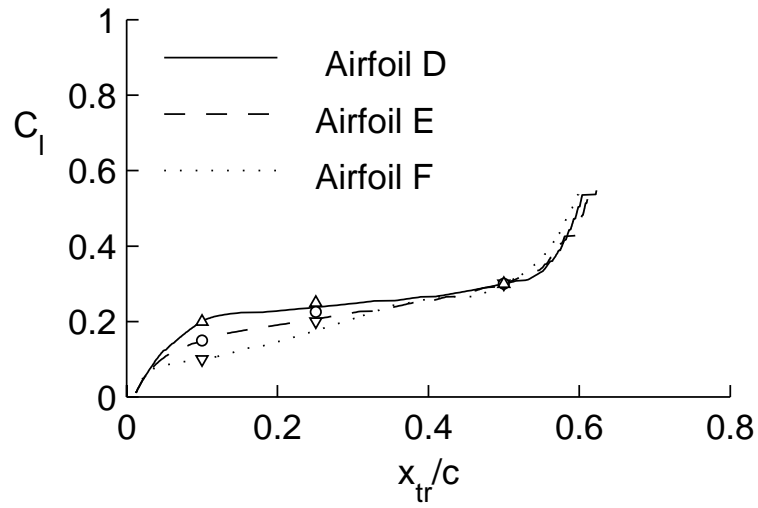


Figure 2.8: Converged lower-surface transition curves for airfoils  $D$ ,  $E$ , and  $F$  calculated using PROFOIL.

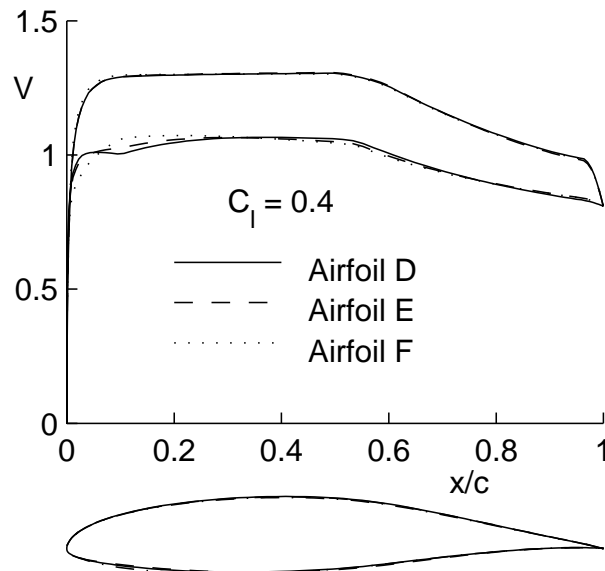


Figure 2.9: Inviscid velocity distributions for airfoils  $D$ ,  $F$ , and  $F$ .

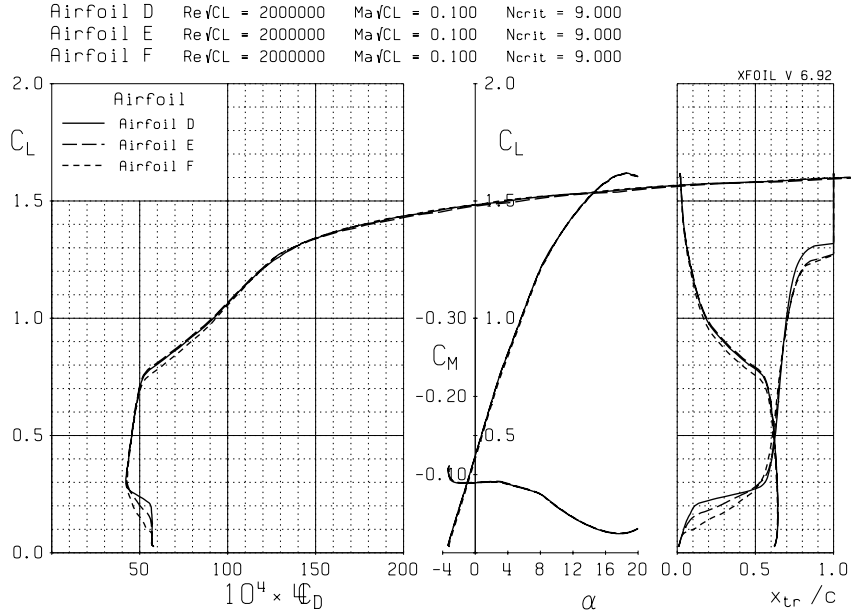


Figure 2.10: Performance of airfoils  $D$ ,  $E$ , and  $F$  predicted using XFOIL.

while the lower corner of the drag bucket is at the same  $C_l$  for the three airfoils, the  $C_l$  for the upper corner increases as the lower corner sharpens. Therefore, by decreasing the slope of the lower-surface transition curve, it is possible to increase the low-speed performance of the airfoil while maintaining the same high-speed performance.

### 2.2.3 Family of NLF Airfoils with Various Amounts of Camber

In the third example, specification of the transition curve is used to control the camber of a family of NLF airfoils ( $G$ ,  $H$ , and  $I$ ). The airfoils were designed by varying the design  $C_l$  for the lower-surface segment, while keeping the slope of the lower-surface transition curve and amount of laminar flow constant. Figure 2.11 shows the converged lower-surface transition curves computed using PROFOIL for the three airfoils. It can be seen that the  $C_l$  for the lower-surface transition curve decreases when progressing from airfoil  $G$  to airfoil  $I$ . Figure 2.12 shows the

shape of the three airfoils as well as the velocity distributions. As the figure shows, changes to the design  $C_l$  for the lower-surface transition curve has a systematic effect on the camber of the airfoil, with airfoil  $G$  having the largest amount of camber.

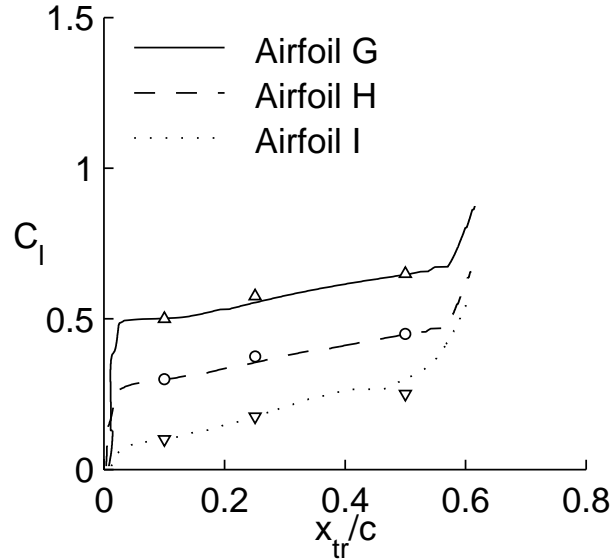


Figure 2.11: Converged lower-surface transition curves for airfoils  $G$ ,  $H$ , and  $I$  calculated using PROFOIL.

The effects on the aerodynamic performance of the airfoils resulting from the above specification are seen in Fig. 2.13. As the figure shows, the  $C_l$  value for the lower corner of the drag bucket is directly related to the  $C_l$  value for the lower-surface transition-curve specification. Furthermore, the pitching moment of the airfoil has been increased in order to maintain similar velocity gradients in the recovery regions of the airfoil. In addition, as the  $C_l$  for the lower corner is increased, the  $C_{lmax}$  of the airfoil is also increased. This behavior is consistent with changes in camber. Thus, by specifying the location of the lower-surface transition curve, the camber of the airfoil can be controlled.

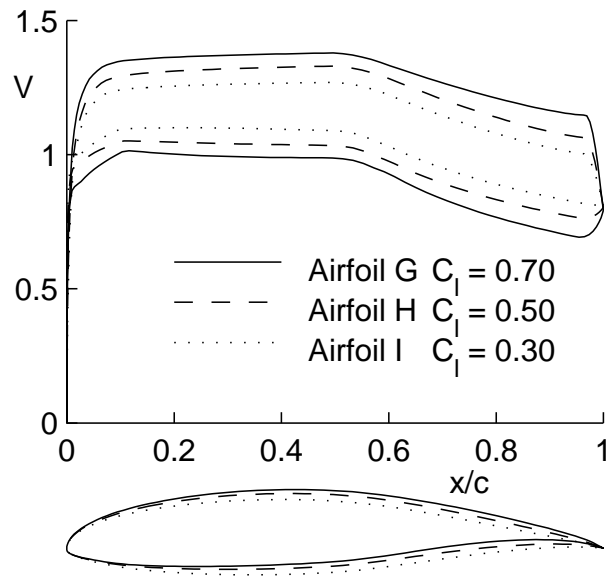


Figure 2.12: Inviscid velocity distributions for airfoils  $G$ ,  $H$ , and  $I$ .

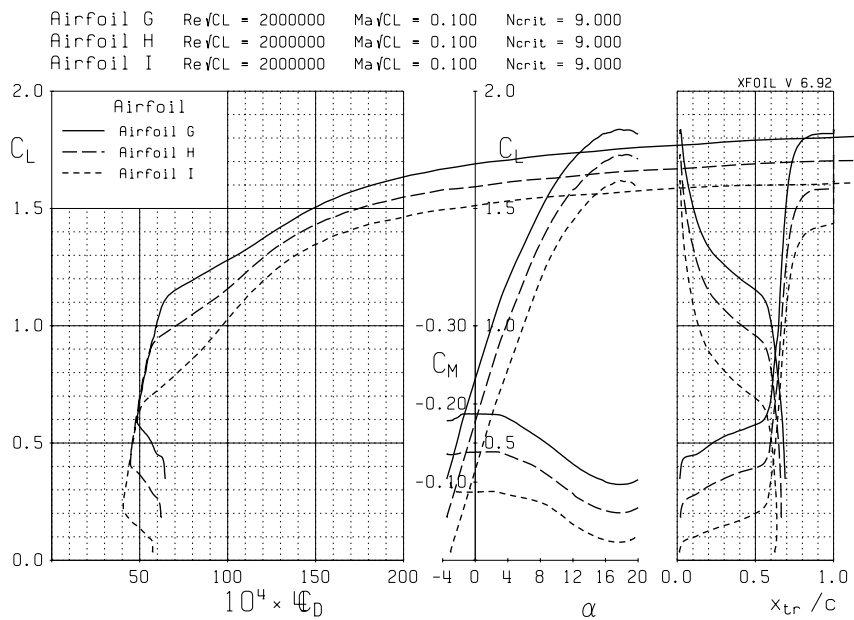


Figure 2.13: Performance of airfoils  $G$ ,  $H$ , and  $I$  predicted using XFOIL.

## 2.2.4 Family of NLF Airfoils with Various Extents of Laminar Flow

In the fourth example, transition-curve specification is used to control the amount of laminar flow over the lower and upper surfaces of a family of airfoils ( $J$ ,  $K$ , and  $L$ ). In this example, simultaneous specifications are made to the transition curves on both the lower and upper surfaces of the airfoil. The airfoils were designed by altering the chordwise extents of the segments for which the transition curves are specified. Figure 2.14 shows the transition-curve specifications as well as the converged upper and lower surface transition curves computed using PROFOIL for the three airfoils. It can be seen that airfoil  $J$  has the largest amount of laminar flow with the design segments extending from  $0.1c$  to  $0.6c$  on both the upper and lower surfaces. For the airfoils  $K$  and  $L$ , the corresponding segments extend from  $0.1c$  to  $0.5c$  and from  $0.1c$  to  $0.4c$  respectively. Downstream of these design segments, the velocity gradients become progressively more adverse. Therefore, the chordwise extents of the design segments determine the extents of laminar flow on the upper and lower surfaces of the airfoil for this family. Figure 2.15 shows the shape of the three airfoils as well as the inviscid velocity distributions. As can be seen, the design specifications result in a systematic variation of the extents of favorable gradients on the airfoil.

The predicted viscous characteristics for the family of airfoils can be seen in Fig. 2.16. As expected, increasing the extent of laminar flow results in decreased drag within the drag bucket. The specification also has an effect on the location of the upper corner of the drag bucket. The airfoil with the largest extent of laminar flow has the lowest upper corner. This example serves to illustrate the capability of the current approach in simultaneously achieving desired transition-curve specifications over different portions of the airfoil.

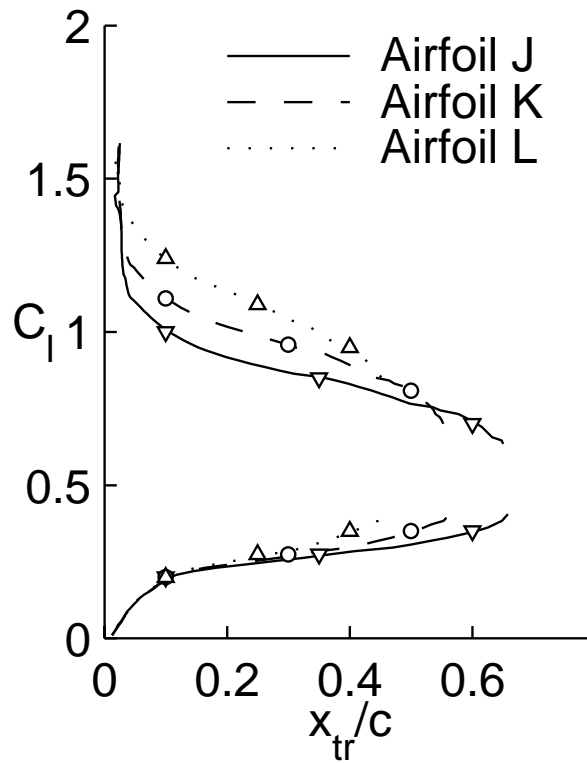


Figure 2.14: Converged lower-surface transition curves for airfoils  $J$ ,  $K$ , and  $L$  calculated using PROFOIL.

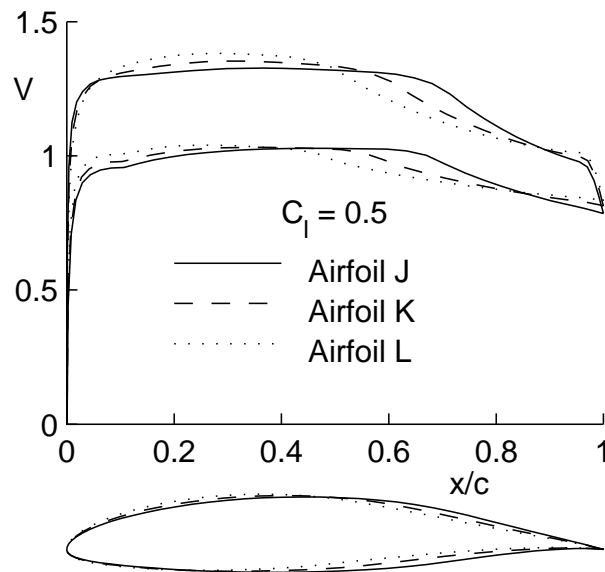


Figure 2.15: Inviscid velocity distributions for airfoils  $J$ ,  $K$ , and  $L$ .

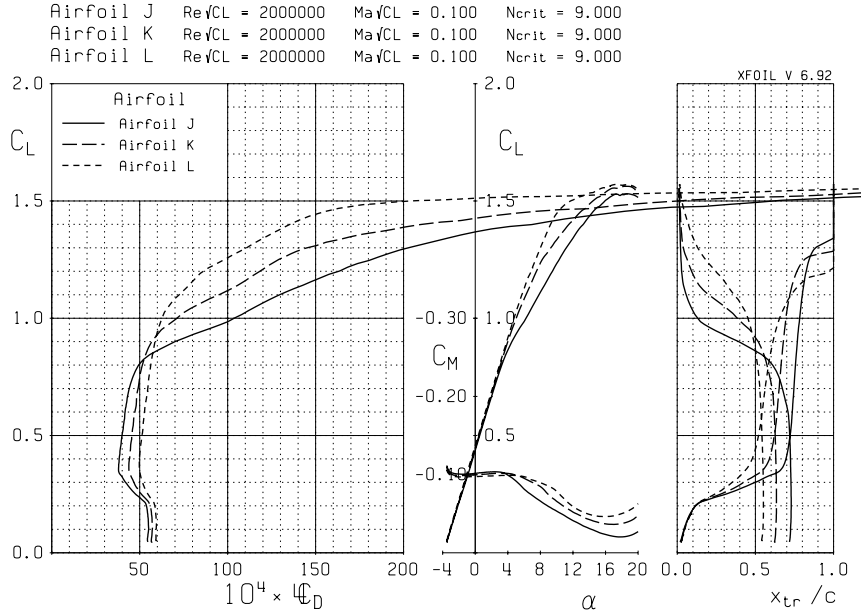


Figure 2.16: Performance of airfoils  $G$ ,  $H$ , and  $I$  predicted using XFOIL.

## 2.3 Summary

An inverse airfoil design approach that uses the boundary-layer transition curve as an input has been presented in this chapter. This method was developed to take advantage of the strong connection between the transition curve and the final airfoil performance. The approach uses a multidimensional Newton iteration to adjust the airfoil velocity distribution in order to achieve the desired specifications.

Four examples were presented in this chapter to demonstrate the usefulness of the approach. In the first example, a single specification to an NLF airfoil was used to validate the results of the method. In the second example, a family of three NLF airfoils was designed with varying transition-curve slopes. This example showed how the shape of the drag bucket can be controlled by transition curve specifications. The third example presented a family of NLF airfoils with various amounts of camber and served to demonstrate how the transition curve can be used to control the location of the drag bucket. Finally, in the fourth example, a family of NLF airfoils with various amounts of camber was designed. This exam-

ple demonstrated the capability of the design approach to simultaneously make specifications to both the upper and lower transition curves. All of these examples demonstrate the benefits of having such an approach in an airfoil designer's toolbox.

## Chapter 3

# Aircraft Performance Considerations in Inverse Airfoil Design

In spite of improvements in inverse airfoil design and airfoil-aircraft matching, the process of tailoring airfoils for an aircraft still relies on numerous post-design aircraft performance simulations. Inverse airfoil design can be made easier if the aircraft performance considerations are incorporated in the airfoil design process. Such an enhancement would result in a more sophisticated approach to inverse airfoil design in which the final application is considered right during the airfoil design stage. For these reasons, the second part of the research, presented in this chapter, aimed at expanding the inverse airfoil design process to include aircraft performance considerations. More specifically, this chapter describes how the aircraft level-flight maximum-speed and maximum-range considerations are incorporated in inverse airfoil design.

The following section provides an overview of the methodology for including aircraft performance considerations in inverse airfoil design. The next section presents a description of the post-design aircraft performance simulation method used for validation. The characteristics of the example aircraft used in this chapter for illustration of the airfoil design process are then presented. The remainder

of the chapter discusses how airfoils can be tailored for various performance considerations.

## 3.1 Methodology

To incorporate aircraft performance considerations in inverse airfoil design, the inverse airfoil design method PROFOIL<sup>10,11</sup> was adapted. Details of the PROFOIL code can be found in Sec. 2.1.1. This section first gives an overview of the design formulation and then discusses the development of the design formulation to incorporate the two aircraft performance considerations (level-flight maximum speed,  $V_{max}$ , and maximum range,  $R_{max}$ ) in the PROFOIL code.

### 3.1.1 Overview of the Design Formulation

To present an overview of the formulation, the drag polar of a representative NLF airfoil, shown in Fig. 3.1, is considered. This polar was obtained by analyzing the airfoil at a constant  $Re\sqrt{C_l}$ . The  $C_l$  values for the upper and lower corners of the LDR,  $C_l^{up}$  and  $C_l^{low}$ , are marked in the Fig. 3.1. Desired values for these lift coefficients for given extents of laminar flow are easily achieved during inverse design by changes to the airfoil camber and thickness, as illustrated in Ref. 17. It was also shown in Refs. 17 and 20 that for changes to the airfoil camber and thickness with a given extent of laminar flow, the points on the polar corresponding to  $C_l^{up}$  and  $C_l^{low}$  move along a locus trajectory that is close to a straight line in the  $C_d$ - $C_l$  plot. This “low-drag curve” is marked in Fig. 3.1 by a dotted line. It is not clear at the airfoil design stage, however, as to what are the most suitable values for the  $C_l^{up}$  and  $C_l^{low}$  in order to match the airfoil to a given aircraft so as to maximize the performance of the aircraft.

Two aircraft performance parameters were considered in this study: level-flight

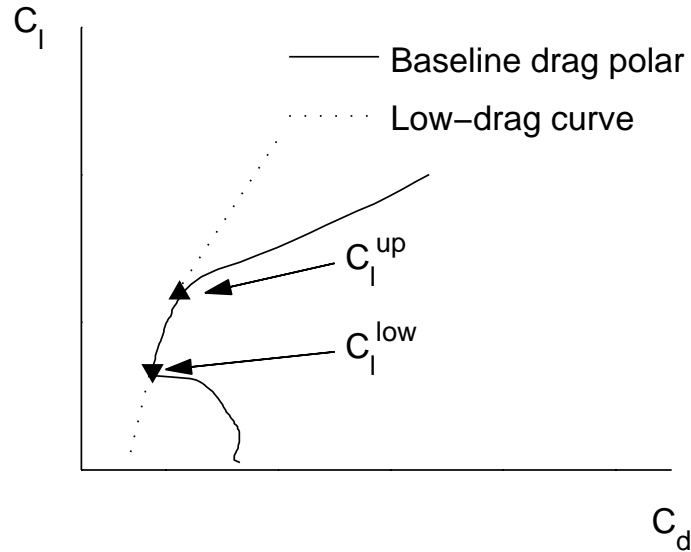


Figure 3.1: Airfoil drag polar used for illustration.

maximum speed,  $V_{max}$ , and maximum range,  $R_{max}$ . Earlier work<sup>20</sup> demonstrated the suitability of the use of the two lift coefficients  $C_l^{up}$  and  $C_l^{low}$  as design variables in order to tailor an NLF airfoil for maximizing these two aircraft performance parameters. When tailoring the airfoil for these performance parameters, the following questions can be posed: (i) what is the best possible value for  $C_l^{low}$  in order to tailor the airfoil for achieving the highest possible  $V_{max}$  without sacrificing low-speed performance? and (ii) what is the best possible value for  $C_l^{up}$  in order to tailor the airfoil for the maximum-range condition without unnecessary penalties at the high-speed conditions? The objective was to formulate the airfoil design problem in order to achieve this airfoil-aircraft matching during the inverse airfoil design stages.

### 3.1.2 Illustration of the Approach

This subsection provides an overview of how an airfoil can be tailored for the  $V_{max}$  and  $R_{max}$  conditions of an aircraft during the inverse design process. For this purpose, a hypothetical aircraft with given wing planform geometry, fuselage

drag, and power characteristics is considered. A baseline airfoil is assumed as the initial choice for the wing and this subsection shows how the camber of the baseline airfoil can be adjusted for tailoring the airfoil for either the  $V_{max}$  or  $R_{max}$  flight conditions.

Figure 3.2 shows the drag polars for the the starting, or baseline, airfoil and for the airfoil tailored for  $V_{max}$ . Also shown in the figure are the locations of  $C_l^{low}$  for both airfoils as well as the low drag line. It is seen that in this example, the tailored airfoil has a lower value of  $C_l^{low}$  than the baseline airfoil. The full-power rate-of-climb ( $ROC$ ) variations for both airfoils are shown in Fig. 3.3. It is seen that by lowering the  $C_l^{low}$  of the baseline airfoil, the value of  $V_{max}$  has increased since  $V_{max}$  is the velocity corresponding to zero  $ROC$ . Not only is the  $V_{max}$  of the baseline airfoil less than the tailored airfoil, but it also occurs outside of the drag bucket. In addition, the  $C_l^{low}$  of the tailored airfoil corresponds to the  $C_l$  value that corresponds to zero  $ROC$ . Therefore, to tailor an airfoil to maximize  $V_{max}$ , the drag bucket should be placed in such a way that the  $C_l^{low}$  corresponds to the condition of zero  $ROC$ . This illustration also provides useful guidelines for incorporating the airfoil-aircraft tailoring for the  $V_{max}$  condition in the inverse design process. A Newton iteration procedure can be used to adjust the design parameters that control the  $C_l^{low}$  until  $C_l^{low}$  corresponds to the  $V_{max}$  condition, i.e. until  $ROC=0$  at  $C_l = C_l^{low}$ .

The drag polars for the baseline airfoil and the airfoil tailored for  $R_{max}$  are shown in Fig. 3.4. Also shown are the low-drag curve and the values of  $C_l^{up}$  for both airfoils. As the figure shows, in this instance, the  $C_l^{up}$  for the tailored airfoil is greater than that for the baseline airfoil. Figure 3.5 shows the variation of aircraft range  $R$  with velocity  $V$  for the two airfoils. It is seen that the tailored airfoil has a greater  $R_{max}$  than the baseline airfoil. Furthermore, the  $R_{max}$  for the baseline airfoil occurs when operating outside of the drag bucket. The ideal value

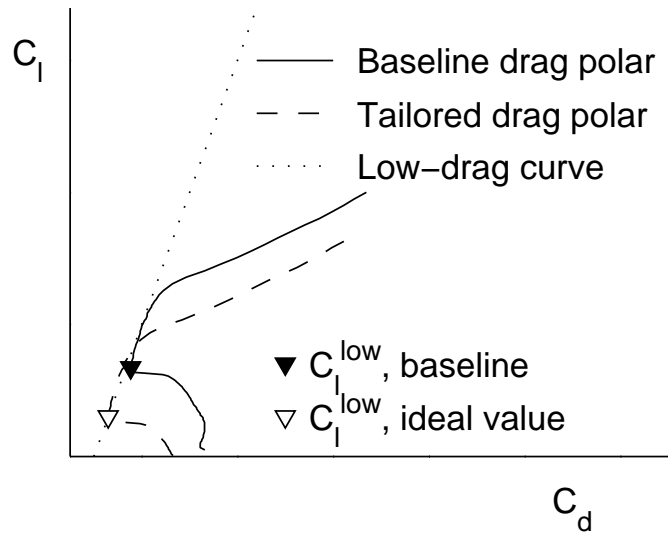


Figure 3.2: Drag polars for the baseline airfoil and the airfoil tailored for  $V_{max}$ .

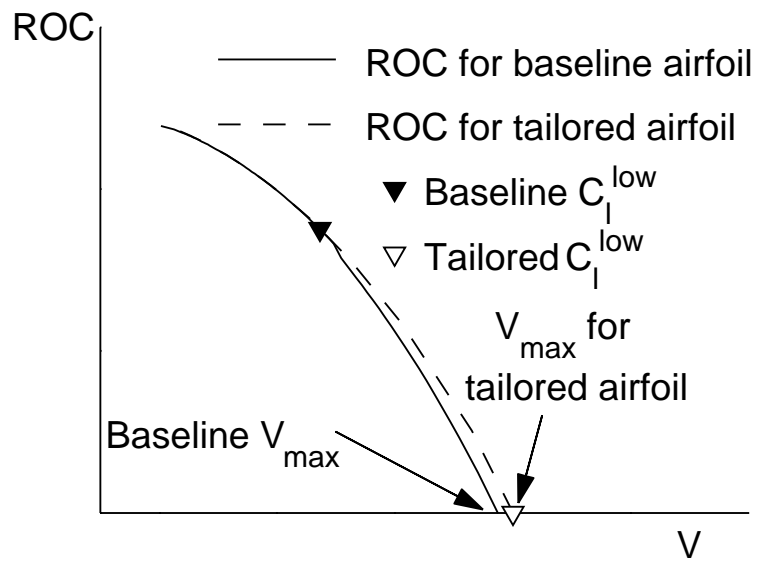


Figure 3.3: Illustration of the effect of the lower corner of LDR on  $V_{max}$ .

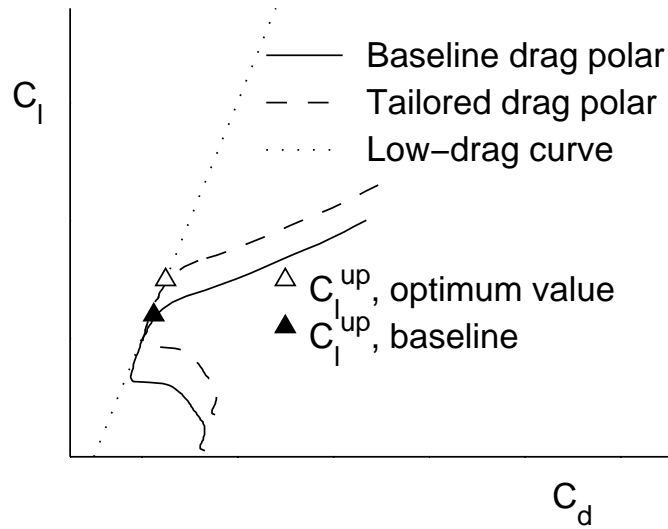


Figure 3.4: Drag polars for the baseline airfoil and the airfoil tailored for  $R_{max}$ .

of  $C_l^{up}$  is found by determining the value of  $C_l$  along the low-drag curve that gives the maximum value of  $R_{max}$ . The tailored airfoil will have a  $C_l^{up}$  that corresponds to this  $C_l$ . This matching can be achieved in the inverse design framework using Newton iteration to adjust the design variables that affect  $C_l^{up}$  until the difference between  $C_l^{up}$  and the ideal value for  $C_l^{up}$  is brought to zero.

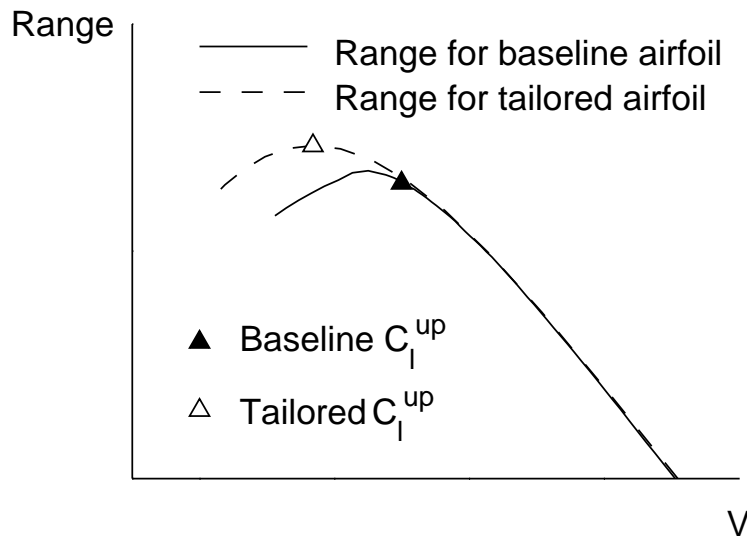


Figure 3.5: Illustration of the effect of the upper corner of LDR on  $R_{max}$ .

### 3.1.3 Airfoil Tailoring for $V_{max}$

As illustrated in Fig. 3.3, an airfoil tailored for the aircraft  $V_{max}$  condition will have  $ROC = 0$  at the flight speed corresponding to  $C_l^{low}$ . In order to examine how to incorporate this in the inverse-design Newton iteration structure, it is necessary to examine the contribution of the airfoil  $C_d$  to the aircraft  $ROC$ . With the assumption that the wing profile drag coefficient is equal to the airfoil  $C_d$ , the aircraft  $C_D$  can be determined by adding the parasite-drag contribution of the fuselage and other components and wing  $C_{D_i}$  to the wing profile drag coefficient, as shown in Eq. 3.1. The resulting aircraft drag, power required for level flight, and rate of climb are presented in Eqs. 3.2, 3.3, and 3.4.

$$C_D = C_d + \frac{C_{Df}S_f}{S_w} + \frac{C_L^2}{\pi eAR} \quad (3.1)$$

$$D = \frac{1}{2}\rho V^2(C_d S_w + C_{Df}S_f) + \frac{2W^2}{\pi b^2 e \rho V^2} \quad (3.2)$$

$$P_{req} = \frac{1}{2}\rho V^3(C_d S_w + C_{Df}S_f) + \frac{2W^2}{\pi b^2 e \rho V} \quad (3.3)$$

$$ROC = \eta_p P_{av} - P_{req} \quad (3.4)$$

The residual for the Newton equation for the  $V_{max}$  tailoring can be posed as shown in Eq. 3.5. For airfoils that are designed by posing the inverse design problem as shown in Ref. 17, the  $C_l^{low}$  is the design  $C_l$  of the lower surface. The  $ROC$  at  $C_l^{low}$  is computed using Eqs. 3.1–3.4 by assuming  $C_L = C_l^{low}$  and computing the resulting  $V$  from the  $C_L$ . The airfoil  $C_d$  is computed at this  $C_l$  by first using the airfoil inviscid velocity distribution along with the direct integral boundary layer method in PROFOIL to determine the locations of the upper-

and lower-surface transition of the laminar boundary layer. The skin-friction drag coefficient is then estimated using flat-plate boundary-layer equations from Ref. 27 for the known extents of laminar and turbulent boundary layers on the upper and lower surfaces of the airfoil. More details of this approximation can be found in Appendix B. Figure 3.6 shows a comparison between the skin-friction drag calculated using the flat-plate method as well as the total airfoil drag obtained from XFOIL analysis. It can be seen that the skin-friction drag closely corresponds to the total drag at  $C_l$  values within the drag bucket. Therefore, the pressure drag contributions are assumed to be negligible for the lift coefficients in the LDR. This approximate method of determining the airfoil  $C_d$  was developed in order to obtain rapid estimates suitable for the potentially large number of function evaluations that could result in the multidimensional Newton iteration scheme for inverse design. The Jacobian for the Newton equation is calculated as shown in Eq 3.6.

$$F = 0.0 - (ROC)_{C_l^{low}} \quad (3.5)$$

$$J_{i,j} = \frac{\partial ROC}{\partial \alpha^*} \quad (3.6)$$

Thus, by posing the design problem as a part of the Newton iteration framework, the inverse method can be used to determine the optimum value of  $C_l^{low}$  for a given aircraft and determine the corresponding airfoil shape. Figure 3.7 shows a flowchart for the process.

### 3.1.4 Airfoil Tailoring for $R_{max}$

An airfoil tailored for the maximum-range flight condition needs to have the  $C_l^{up}$  equal to the optimum  $C_l^{up}$ , as illustrated earlier in Fig. 3.5. The equation for range  $R$  at any given  $C_l$  is shown in Eq. 3.7. When this airfoil design problem is

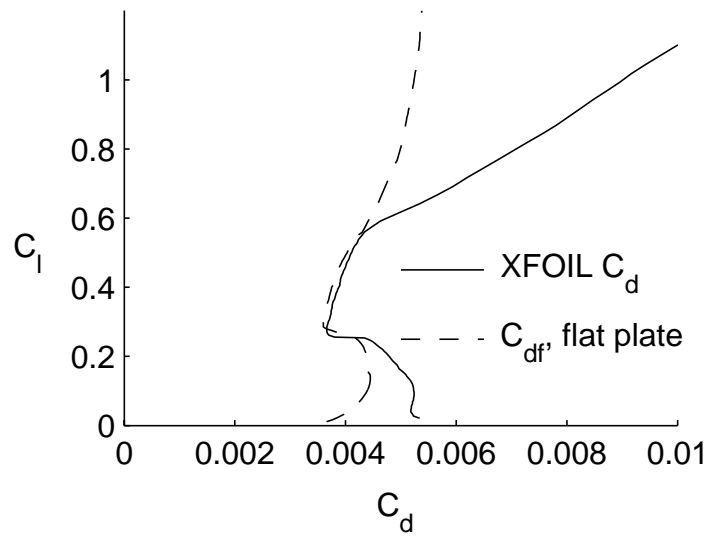


Figure 3.6: Comparison between flat plate drag and total drag at  $Re\sqrt{C_l} = 3.42 \times 10^6$

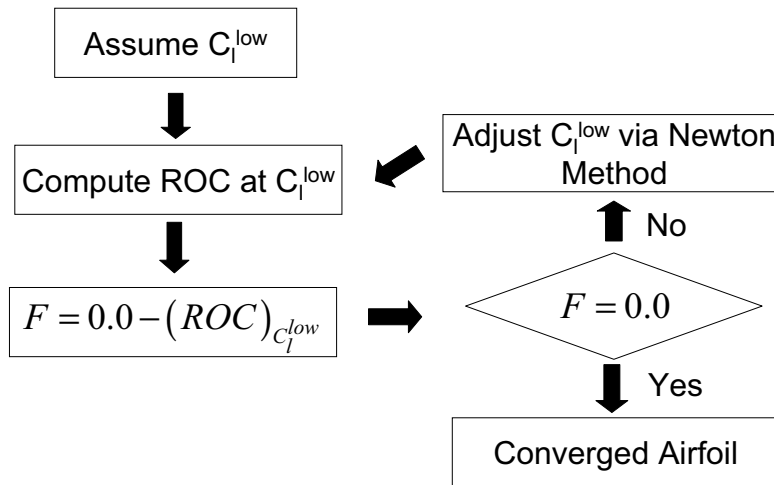


Figure 3.7: Flowchart of  $V_{max}$  tailoring routine.

incorporated in the Newton iteration in PROFOIL, the equation for the residual for this Newton equation is shown in Eq. 3.8. The Jacobian is calculated using Eq. 3.9. The aircraft  $C_D$  is computed using Eq. 3.1, for which the airfoil  $C_d$  is estimated using the flat-plate boundary-layer skin-friction equations. In this case also, the pressure drag contributions of the airfoil are assumed to be small as the airfoil is operating within the drag bucket.

$$R = \frac{\eta}{SFC} \frac{C_L}{C_D} \int_{W_e}^{W_f} \frac{dW}{W} \quad (3.7)$$

$$F = (C_l^{up})_{opt} - C_l^{up} \quad (3.8)$$

$$J_{i,j} = \frac{\partial C_l^{up}}{\partial \alpha^*} \quad (3.9)$$

The determination of the value of  $C_l^{up}$  within the PROFOIL code is not straightforward. Unlike with the lower surface, the values for the  $\alpha^*$  for the segments on the upper surface vary significantly from the leading edge to the trailing edge.<sup>17</sup> For this reason, the  $C_l^{up}$  for the initial airfoil is first determined by generating a drag polar using XFOIL. This value is provided as an input to the PROFOIL code. As the  $\alpha^*$  values for the upper-surface segments are adjusted in the Newton iteration process, the value of  $C_l^{up}$  is adjusted accordingly using a gradient of 0.1 change in  $C_l^{up}$  for every degree change in the upper-surface  $\alpha^*$ . For the determination of  $(C_l^{up})_{opt}$ , an approximation to the equation for the low-drag line is obtained by use of finite differencing to determine the change in airfoil skin-friction  $C_d$  for a given change in  $C_l^{up}$ . This equation for the low-drag line is used in the code to determine  $(C_l^{up})_{opt}$ . A flowchart for the method is shown in Fig. 3.8.

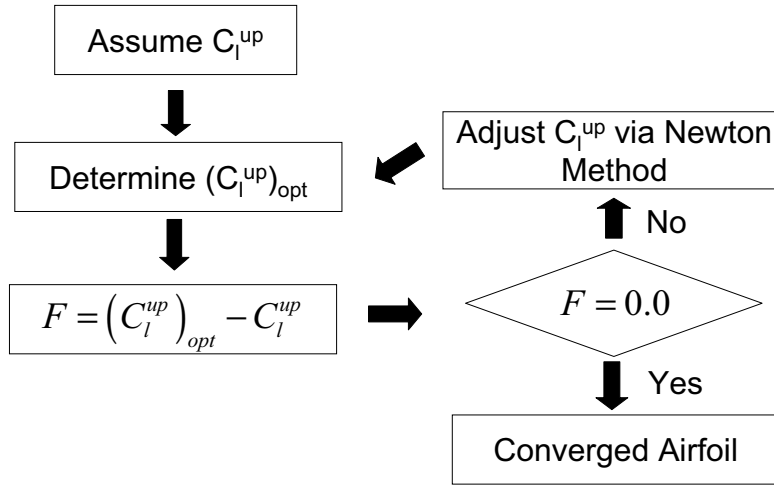


Figure 3.8: Flowchart of  $R_{max}$  tailoring routine.

The use of such approximations in  $C_l$  and  $C_d$  in the design formulation enables rapid design via the Newton iteration process. It must be mentioned that the objectives in the design formulation are only to determine the best values for  $C_l^{up}$  and  $C_l^{low}$  and not to predict the resulting values of  $V_{max}$  and  $R_{max}$ . For these objectives, the approximations are not only valid, but also enable rapid, interactive design.

## 3.2 Analysis Tools for Validation

This section describes the tools and methodology used to validate the results obtained using the PROFOIL code. The first step in the approach was to analyze the converged airfoil using XFOIL to calculate the drag polar of the airfoil in order to obtain values for both pressure and friction drag.

Once the airfoil drag polar was calculated, the Wings<sup>20</sup> code was used to cal-

culate the trimmed induced and profile drag of the lifting surfaces of the aircraft. Wings is a vortex lattice code that can handle multiple lifting surfaces. The code reads in the XFOIL  $\alpha$ - $C_l$ - $C_d$ - $C_m$  polar output files to allow for the use of the airfoil drag polar and pitching moment curves for various sections along the wing span. In the current analysis, the incidence of the tail at each angle of attack is adjusted to trim the aircraft, i.e.  $C_{Mc.g} = 0.0$ . This ensures that the aircraft performance will be calculated with the full drag that the aircraft generates in trimmed level flight.

After the total drag of the aircraft is calculated, the performance of the aircraft can be calculated using PERF.<sup>20</sup> PERF is an aircraft performance simulation code which uses the equations in Secs. 3.1.3 and 3.1.4 along with the drag output from the Wings code to calculate the aircraft rate of climb and range at each angle of attack. This method was used to generate all of the performance plots in Sec. 3.4 in order to validate the results obtained from the inverse design method. It should be noted that this method was not used in any part of the design method itself.

### 3.3 Aircraft Specifications

This section presents the relevant details of a hypothetical general aviation aircraft used in the rest of the paper. The aircraft is a conventional, aft-tail configuration with a constant-speed propeller driven by a piston engine. The planview of the wing and tail of the aircraft is shown in Fig. 3.9.

Table 3.1 provides the relevant specifications for the aircraft. As shown, an equivalent parasite drag area ( $C_{Df}S_f$ ) was assumed for the fuselage and all the components of the airplane except the wing. The propeller efficiency was assumed to have the non-linear distribution shown in Fig. 3.10. The static margin for the hypothetical aircraft was assumed to be 15% of the wing mean aerodynamic chord.

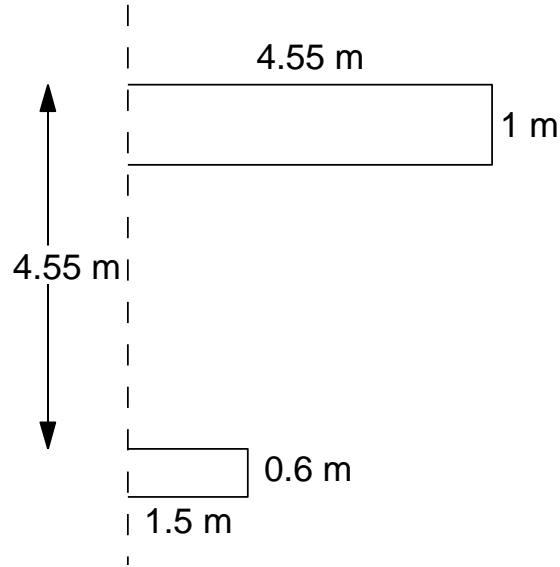


Figure 3.9: Planview showing the right-side geometry of the wing and tail for hypothetical aircraft.

### 3.4 Demonstration

For the demonstration of the method, a baseline NLF airfoil was used as an initial candidate wing section for the general aviation aircraft shown earlier in Fig. 3.9. This baseline airfoil was designed using the methodology described in Ref. 17 for the reduced Reynolds number  $Re\sqrt{C_l}$  of 3.42 million. This reduced Reynolds number corresponds to level flight at standard sea level conditions for the aircraft. The airfoil was designed to support at least 50% laminar flow on the upper and lower surfaces when operating in the LDR. The  $\alpha^*$  for the lower surface was set at 2.5 deg, resulting in the lower-surface design  $C_l$  of 0.25. This specification resulted in a  $C_l^{low}$  of 0.25 for the drag polar at this reduced Reynolds number. The thickness-to-chord ratio was specified to be 14% and was achieved by iterating on the  $\alpha^*$  values for the segments on the upper surface. As a result of these specifications, the  $C_l^{up}$  for this polar is 0.5.

Table 3.1: Assumed geometry, drag, and power characteristics for the hypothetical general aviation airplane.

Parameter	Value
Gross Weight ( $W$ )	14269 N (3200 lbf)
Wing reference area ( $S_w$ )	9.10 $m^2$ (97.92 sq.ft.)
Wing aspect ratio (AR)	9.1
Equivalent parasite drag area of airplane minus wing ( $C_{Df}S_f$ )	0.1647 $m^2$ (1.772 sq.ft.)
Rated engine power ( $P_{av}$ )	261 $kW$ (350 hp)
Specific fuel consumption ( $sfc$ )	$8.31 * 10^{-7}$ N/s/W (0.5 lbf/h/hp)
Propeller efficiency ( $\eta_p$ )	85%, constant
Fuel volume	341 liters (90 U.S. gallons)

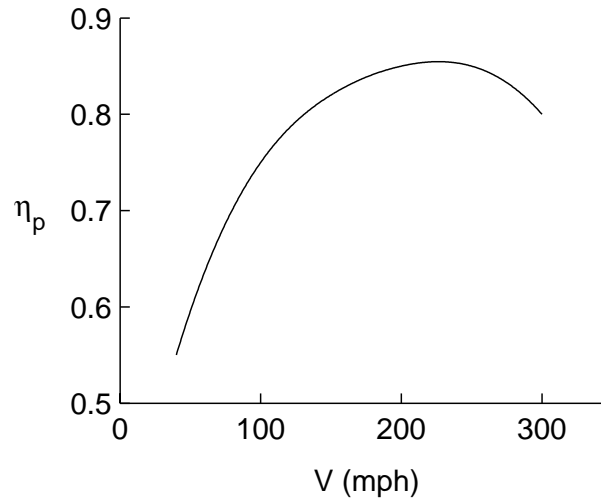


Figure 3.10: Assumed propeller efficiency distribution.

### 3.4.1 Airfoil Tailoring for $V_{max}$

For tailoring the airfoil to suit the aircraft  $V_{max}$  condition, the  $\alpha^*$  values of the lower-surface segments were varied using the Newton iteration scheme described earlier in Sec. 3.1.3. The maximum thickness ratio was maintained at 14%. As a result, changes to the airfoil are similar to changes to the maximum camber. The geometry and inviscid velocity distributions for the baseline airfoil and the converged airfoil (labeled M) are shown in Fig. 3.11. It is seen that the converged airfoil has a lower camber as a result of satisfying the specifications. The drag polars from XFOIL analysis for the baseline and converged airfoils are shown in Fig. 3.12. It is seen that the  $C_l^{low}$  for the converged airfoil M is 0.15, and was determined by the method as an outcome of tailoring the airfoil for the  $V_{max}$  condition. The rate of climb curve for the baseline and converged airfoils are shown in Fig. 3.13. As the figure shows, the converged airfoil has a higher  $V_{max}$ , as seen by the higher velocity at which  $ROC=0$  for the airfoil M.

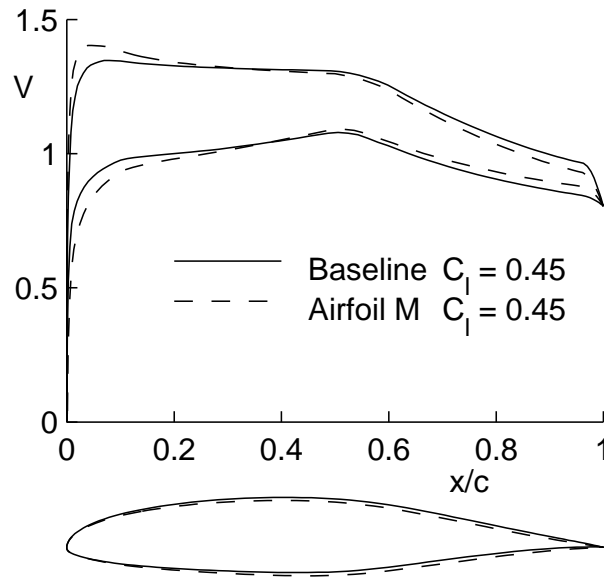


Figure 3.11: Geometries and inviscid velocity distributions for the baseline airfoil and the converged airfoil M.

While the converged airfoil does indeed have a higher  $V_{max}$  than the baseline

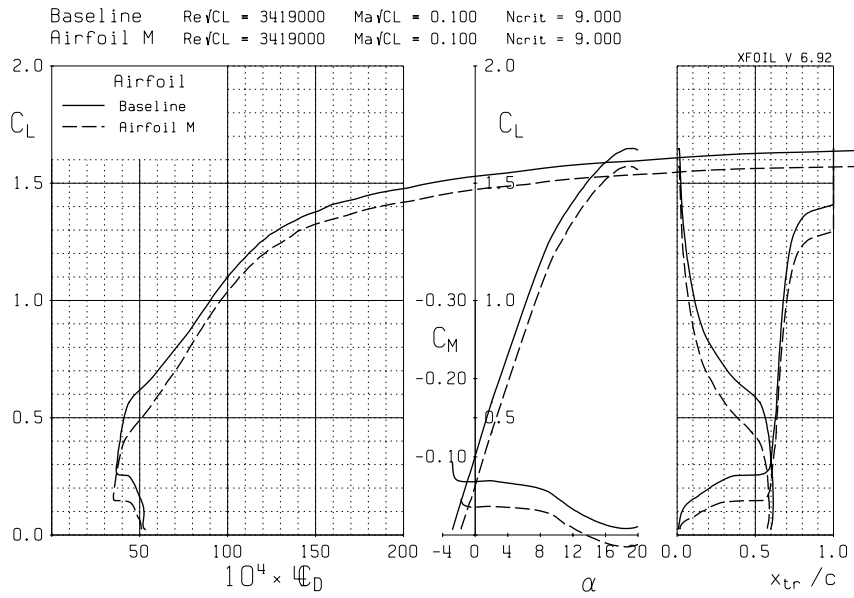


Figure 3.12: Polars for the baseline airfoil and the converged airfoil M from XFOIL analysis.

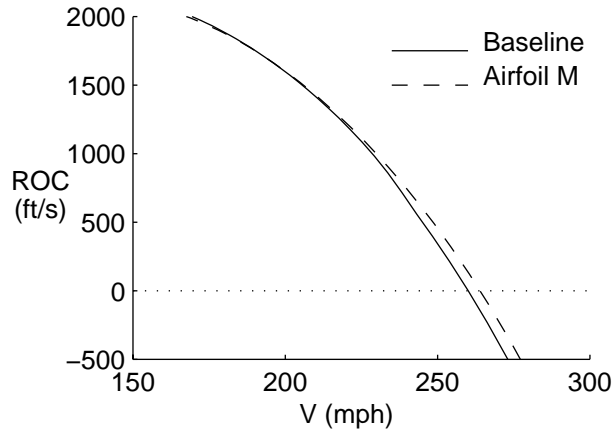


Figure 3.13: Rate of climb curves for the baseline airfoil and the converged airfoil M.

airfoil, it is not evident from the information in Figs. 3.11–3.13 that the airfoil M is necessarily the one that is ideally tailored for the  $V_{max}$  condition. To examine this situation, a family of airfoils with different values of  $C_i^{low}$  was designed around airfoil M. Airfoils M1 and M2 were designed to have  $C_i^{low}$  less than 0.15, and airfoils M3–M5 were designed to have  $C_i^{low}$  greater than 0.15. The drag polars for airfoils M, M1, and M5 are shown in Fig. 3.14. Also marked in the figure are the  $C_i^{low}$  values for the three airfoils. Figure 3.15 shows the variation of the  $V_{max}$  as a function of the airfoil  $C_i^{low}$ . It is seen that as  $C_i^{low}$  is decreased from 0.3, the  $V_{max}$  increases progressively up to a value of the  $C_i^{low}$  of 0.15 corresponding to the  $C_i^{low}$  for the converged airfoil M. Any decrease in  $C_i^{low}$  beyond that for airfoil M results in a zero or small decrease in the  $V_{max}$ . The reason for this trend is that the airfoils M3–M5 have too high a  $C_i^{low}$  and the airfoils M1 and M2 have too low a  $C_i^{low}$  for the aircraft under consideration. The fact that airfoil M is ideally tailored for  $V_{max}$  is reinforced by examining Fig. 3.16, which shows the rate-of-climb curves for M, M1, and M5. It is seen that airfoil M5 has a lower  $V_{max}$  than that of airfoil M, whereas airfoil M1 does not have a larger  $V_{max}$ . Furthermore, the  $V_{max}$  for M5 occurs outside of the drag bucket. This post-design study of the effect of camber on  $V_{max}$  demonstrates that the design formulation successfully tailors the airfoil for the  $V_{max}$  flight condition.

### 3.4.2 Airfoil Tailoring for $R_{max}$

For tailoring the airfoil to suit the aircraft  $R_{max}$  condition, the  $\alpha^*$  values of the lower-surface segments were varied using the Newton iteration scheme described earlier in Sec. 3.1.4. The maximum thickness ratio was maintained at 14%. Although it is the upper corner of the polar that directly controls the maximum range, varying the lower-surface  $\alpha^*$  and maintaining the maximum thickness specification is essentially equivalent to a variation of the  $C_i^{up}$ . As a result, changes

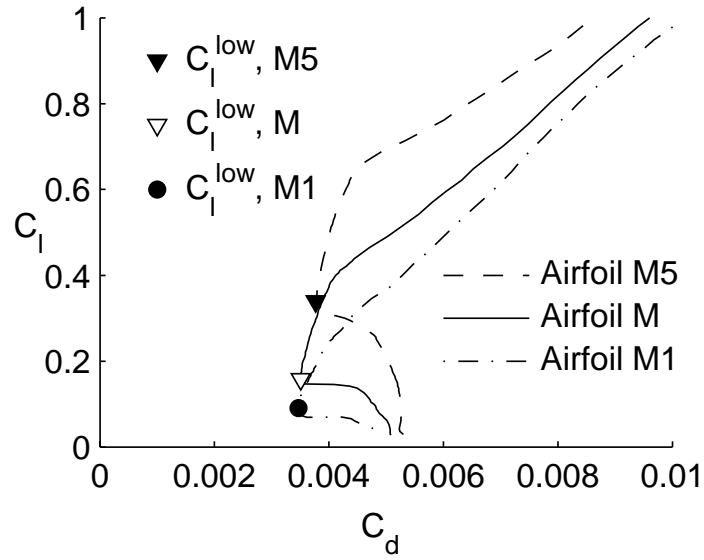


Figure 3.14: Drag polars for airfoils M, M1, and M5

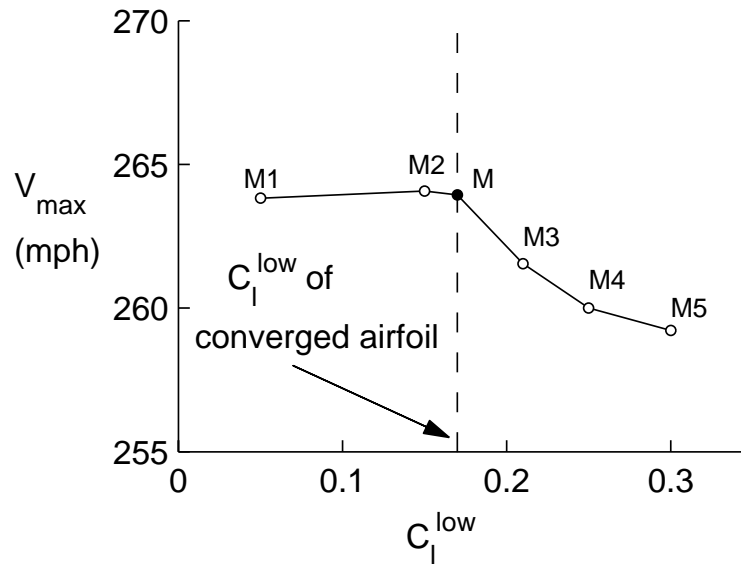


Figure 3.15:  $V_{\text{max}}$  as a function of  $C_l^{\text{low}}$ .

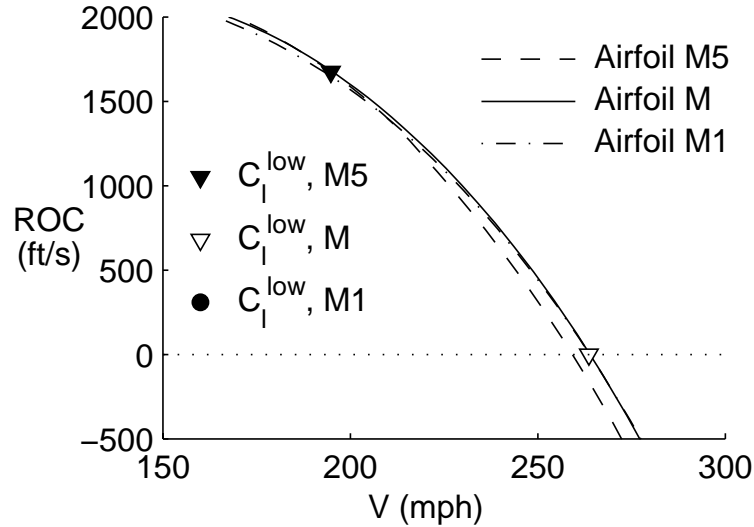


Figure 3.16: Rate of climb curves for airfoils M, M1, and M5

to the airfoil are similar to changes to the maximum camber. The geometry and inviscid velocity distributions for the baseline airfoil and the converged airfoil (labeled N) are shown in Fig. 3.17. It is seen that the converged airfoil N has a higher camber as a result of satisfying the Newton equation in Eq. 3.8. The drag polars for the baseline and converged airfoil N are shown in Fig. 3.18. It is seen that the  $C_l^{up}$  for the converged airfoil N is approximately 0.8. The variations of the aircraft range with  $V$  for the baseline and converged airfoils are shown in Fig. 3.19. As the figure shows, the converged airfoil N has a higher  $R_{max}$  than the baseline airfoil.

To further demonstrate that the converged airfoil N indeed has the optimum camber for maximizing range, a family of airfoils with varying camber (and hence varying values of  $C_l^{up}$ ) were designed around airfoil N. Airfoils N1–N3 have lower camber than airfoil N and airfoils N4 and N5 have progressively higher camber. Figure 3.20 shows the drag polars for airfoils N, N1, and N5 as well as the values of  $C_l^{up}$  for the three airfoils. Figure 3.21 shows the variation of  $R_{max}$  as a function of  $C_l^{up}$  for this family of airfoils. As the figure shows, the range increases with increasing  $C_l^{up}$  up to a certain point corresponding to the  $C_l^{up}$  of airfoil N. After

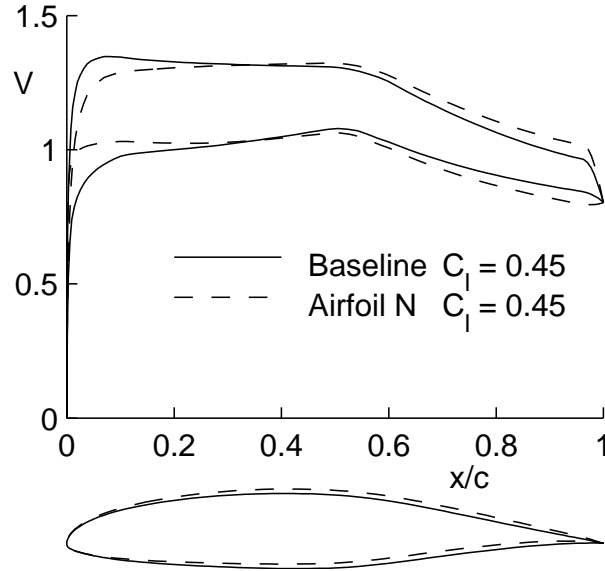


Figure 3.17: Geometries and inviscid velocity distributions for the baseline airfoil and the converged airfoil N.

that point, further increase in  $C_l^{up}$  does not have an effect on the maximum range of the aircraft. It can also be seen from Fig. 3.21 that the converged airfoil N is the optimum for  $R_{max}$ . This is further demonstrated in Fig 3.22, which shows the range curves for airfoils N, N1, and N5. As the figure shows, airfoil N1 has a lower  $R_{max}$  than than airfoil N and airfoil N5 does not have any increase in  $R_{max}$  over N. Furthermore, the  $R_{max}$  of N1 occurs outside the drag bucket. This post-design study of the effect of  $C_l^{up}$  on  $R_{max}$  demonstrates that the design formulation is successful in identifying the optimum camber for an airfoil tailored for the  $R_{max}$  condition.

### 3.4.3 Airfoil Tailoring for $V_{max}$ and $R_{max}$

For the third part of the demonstration of the method, the baseline airfoil was again used as a starting point and the  $\alpha^*$  values for lower-surface segments were adjusted to tailor the lower surface for the  $V_{max}$  condition, while the  $\alpha^*$  values for upper-surface segments were simultaneously adjusted to tailor the upper surface

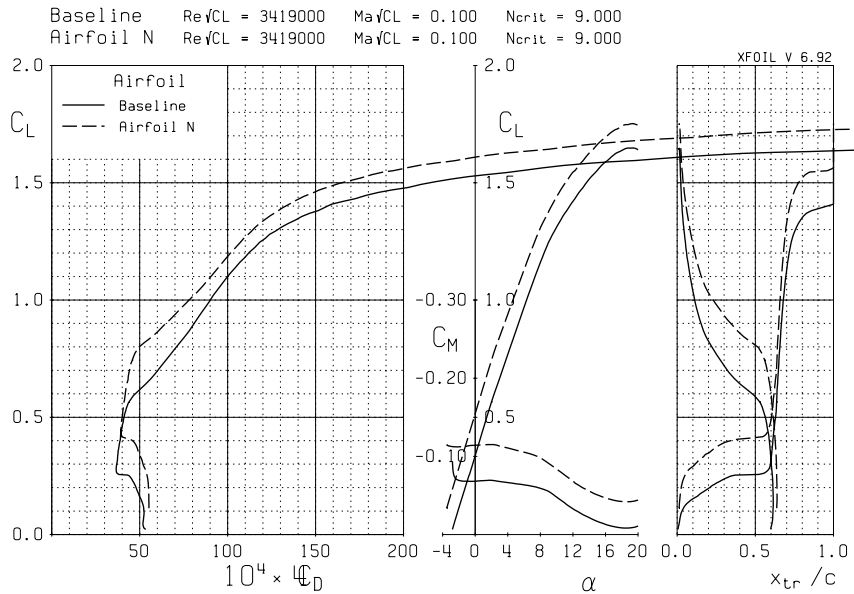


Figure 3.18: Polars for the baseline airfoil and the converged airfoil N from XFOIL analysis.

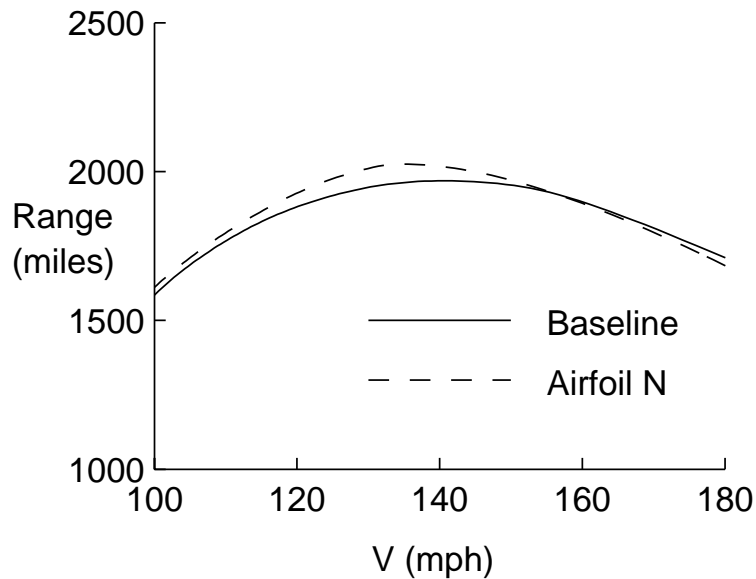


Figure 3.19: Range curves for the baseline airfoil and the converged airfoil N.

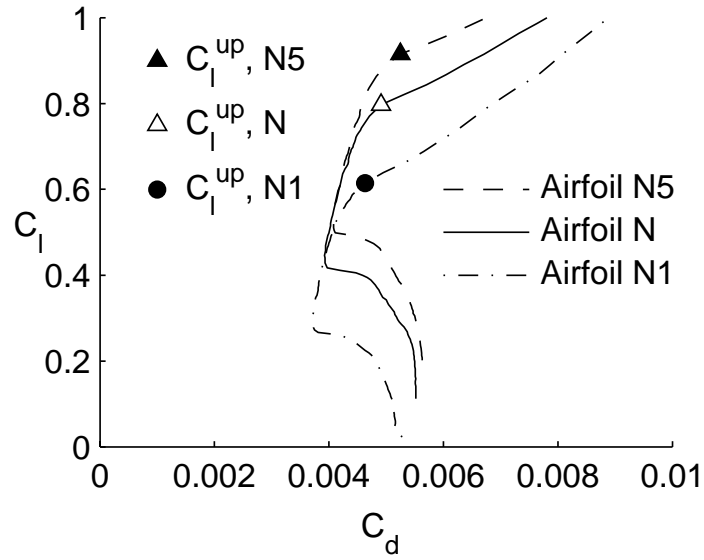


Figure 3.20: Drag polars for airfoils N, N1, and N5

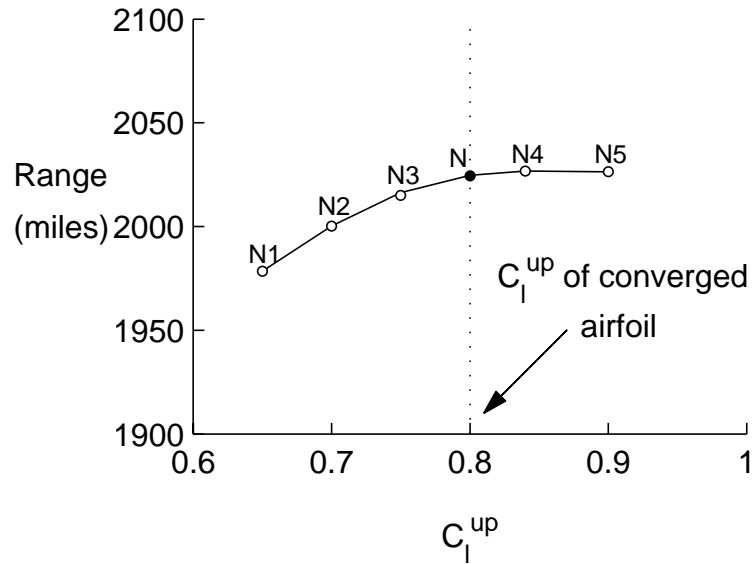


Figure 3.21: Maximum range as a function of  $C_l^{up}$ .

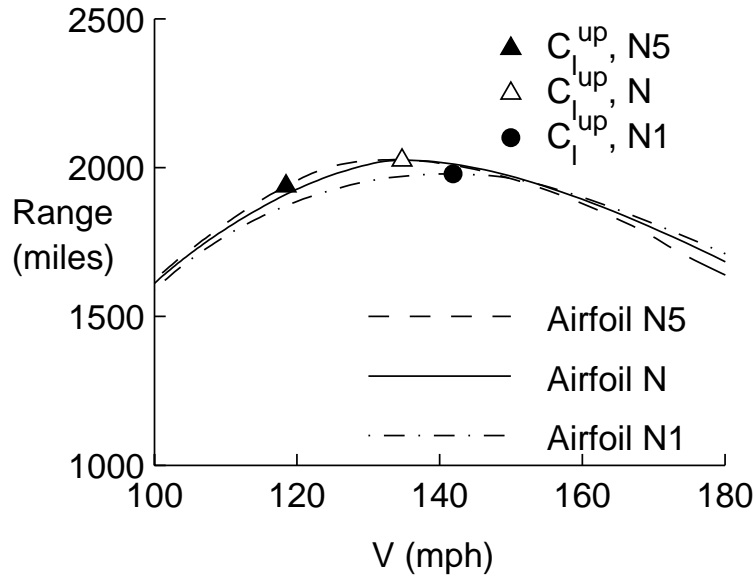


Figure 3.22: Rate of climb curves for airfoils N, N1, and N5

for the  $R_{max}$  condition. Because both the specifications were being satisfied, the thickness ratio was left unspecified and was determined as an outcome of the method. The geometries and inviscid velocity distributions for the baseline airfoil and the converged airfoil (labeled O) are shown in Fig. 3.23. As the figure shows, the converged airfoil has a higher thickness ratio than the baseline airfoil. The drag polars for the baseline and converged airfoil O are shown in Fig. 3.24. It is seen that airfoil O has  $C_l^{low} = 0.11$  and  $C_l^{up} = 0.80$ . It is, therefore, tailored for both the  $V_{max}$  and the  $R_{max}$  conditions. The consequence of the increased thickness ratio, however, is that it has increased  $C_d$  in the middle of the LDR due to larger pressure drag.

Figures 3.25 and 3.26 show the rate-of-climb and range variations for the baseline airfoil and the converged airfoil O. The results clearly show that the converged airfoil O has an improvement in both  $V_{max}$  and  $R_{max}$  over the baseline airfoil. This demonstration shows that the multidimensional Newton formulation is successful in simultaneously accounting for multiple performance considerations in tailoring an airfoil to suit an aircraft.

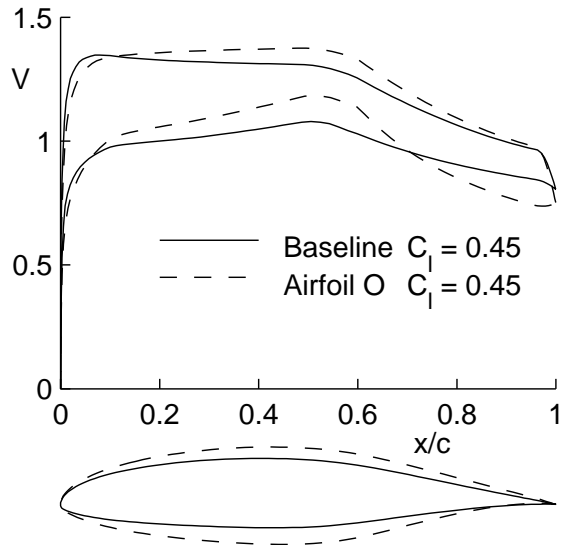


Figure 3.23: Geometries and inviscid velocity distributions for the baseline airfoil and the converged airfoil O.

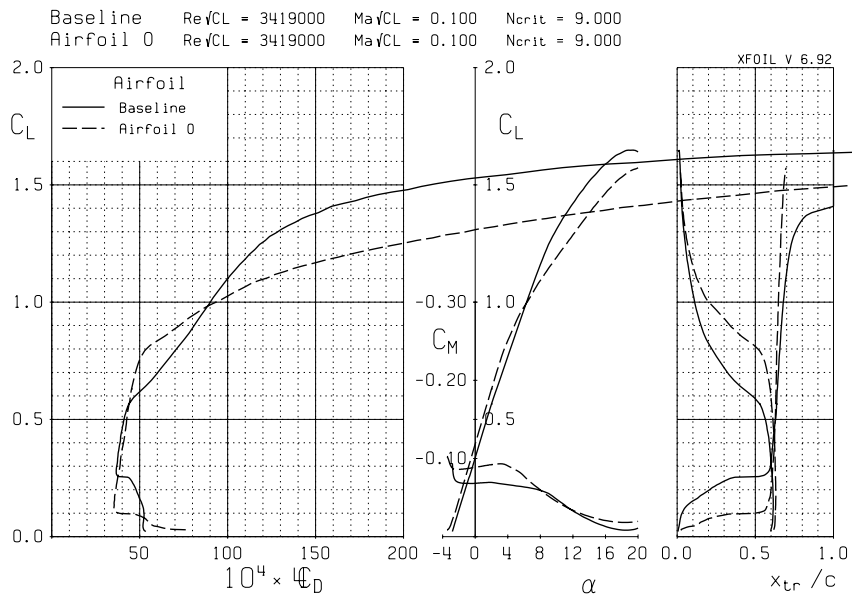


Figure 3.24: Polars for the baseline airfoil and the converged airfoil O from XFOIL analysis.

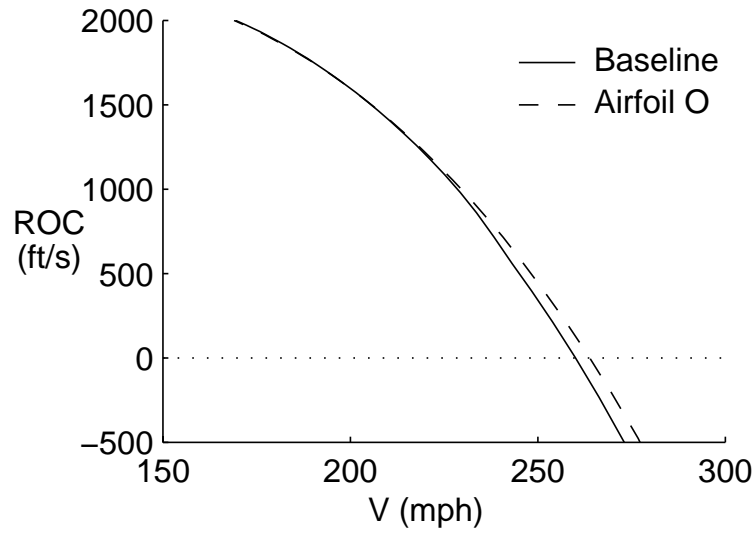


Figure 3.25: Rate of climb curves for the Baseline airfoil and the converged airfoil O.

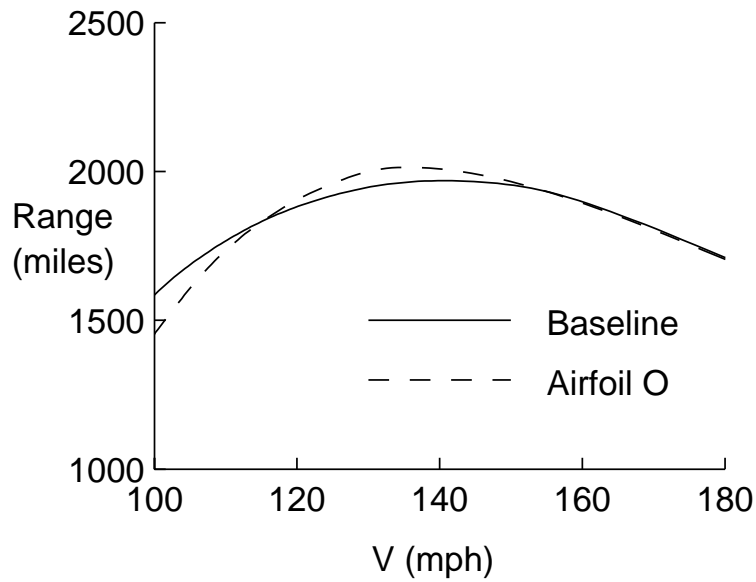


Figure 3.26: Range curves for the Baseline airfoil and the converged airfoil O.

## 3.5 Discussion of Results

This chapter presented an inverse airfoil design approach which incorporates aircraft performance considerations. The method makes the process of airfoil-aircraft matching considerable easier by taking into consideration the final application in the airfoil design. The two aircraft performance parameters considered are  $V_{max}$  and  $R_{max}$ . The method uses a multidimensional Newton iteration to tailor the airfoil for the two considerations.

Three examples were presented to demonstrate the method. In the first example, an NLF airfoil was tailored for  $V_{max}$ . The results of this example were validated using post-design analysis that showed that the tailored airfoil did achieve the maximum possible  $V_{max}$ . The second example presented an NLF airfoil that was tailored for  $R_{max}$ . Again the results were validated and it was shown that the final airfoil achieved the maximum value of  $R_{max}$ . Finally, the third example showed an NLF airfoil tailored for both  $V_{max}$  and  $R_{max}$ . This example served to demonstrate the possibility of tailoring a single airfoil for multiple performance considerations. These three examples demonstrate the usefulness of this method for a designer.

# Chapter 4

## Concluding Remarks

### 4.1 Summary of Research

Inverse airfoil design methods enable a designer to obtain an airfoil shape that satisfy desired aerodynamic and geometric specifications. Many of the early methods were single-point methods; i.e., they were limited to specifications at only one operating condition. Advances have since been made to allow for design at multiple operating conditions via multipoint inverse design methods. The PROFOIL code is one such method that has been successfully used in a variety of airfoil design scenarios.<sup>14-18,28,29</sup> The research presented in this thesis makes two important contributions to the current state of inverse airfoil design. In the first part, an inverse method was developed that allows for the specification of the boundary-layer transition curve. The second part, aircraft performance considerations are incorporated in inverse airfoil design.

#### 4.1.1 Boundary-Layer Transition Curve Specification

The first part of this research presents a method that builds on PROFOIL to allow for specification of the transition curve as an input for inverse airfoil design. The motivation for this research was that much of the final airfoil performance

such as the shape of the drag polar is closely related to the shape of the transition curve. Using a multidimensional Newton iteration, the velocity distribution over a segment is adjusted in the current work to satisfy the specifications to the transition curve. In doing this, the method can be used to successfully design an airfoil that satisfies the desired transition curve. The examples presented show the usefulness of such a method. The current extension also results in a departure from single-point and multipoint design specifications. Because the current method can achieve a desired transition curve, the approach allows for a single design specification that spans multiple operating points. As illustrated by the examples in the paper the new capability is likely to be a useful addition to an airfoil design toolbox.

#### **4.1.2 Incorporation of Aircraft Performance**

##### **Considerations**

Although there has been a steady development of inverse airfoil design methods and airfoil families with specific lift, drag, and moment characteristics and geometry constraints, there has been comparatively less attention paid to tailoring an airfoil to suit an aircraft application. Designing an airfoil to maximize one or more aircraft performance parameters has traditionally required a trial-and-error process, in which the designer iterates between airfoil design and analysis and computation of the resulting aircraft performance. With an objective of shortening the airfoil-aircraft design integration time, a design formulation has been presented in the second part of this thesis that incorporates aircraft performance considerations in laminar-airfoil inverse design. Two aircraft performance parameters have been considered: level-flight maximum speed and maximum range. The design problem is then posed in the form of two questions: (i) what is the optimum

lift coefficient for the lower corner of the airfoil drag bucket in order to tailor the airfoil for the aircraft level-flight maximum speed condition? and (ii) what is the optimum lift coefficient for the upper corner of the airfoil drag bucket in order to tailor the airfoil for the maximum range flight condition?

The second part of this research presents a design formulation that allows for the incorporation of these design considerations in a multidimensional Newton iteration framework available in the PROFOIL inverse airfoil design code. In this Newton iteration process, the conformal-mapping variables that control the lift coefficients for the upper and lower corners of the airfoil drag bucket are automatically adjusted in order to tailor the airfoil for one or both of these two aircraft flight conditions. As a result, the airfoil lower-surface aerodynamics are tailored so that the aircraft rate of climb is zero when the airfoil is operating at the lower corner of the low-drag range and likewise the airfoil upper-surface aerodynamics are tailored for the maximum-range flight condition. When the airfoil with a specified maximum thickness ratio is tailored for one of these conditions, the method determines the optimum camber. When the airfoil is tailored for both these flight conditions, both camber and thickness are determined as an outcome of the design. The results of the inverse design have been validated by post-design studies using aircraft performance computations. The current design formulation represents a new direction in the development of inverse airfoil design methods. Departing from the traditional effort of specifying the desired aerodynamics as input to the inverse design process, the current formulation in addition allows for the specification of the desired performance characteristics of the aircraft as input and the determination of the aerodynamic specifications as well as the airfoil geometry as the outcome of the inverse design process.

## 4.2 Future Work

### 4.2.1 Incorporation of Constant-Landing-Speed Option

The current approach for incorporating the aircraft performance into the airfoil design keeps the wing planform constant. As a result of this, the landing speed of the aircraft will change when the airfoil is tailored. This effect can be seen in Fig. 4.1. The figure shows the lift curve for the baseline airfoil and the airfoil M from Sec. 3.4.1. It can be seen that the tailored airfoil M has a lower  $C_{l_{max}}$  than the starting airfoil. This will result in the aircraft having a higher landing speed. To counteract this, an option to keep the planform variable while keeping  $C_{l_{max}}$  constant is currently being implemented into the method. With this option, the design method will not only determine the proper location of the drag bucket but it will also determine the wing planform as a result of the design method.

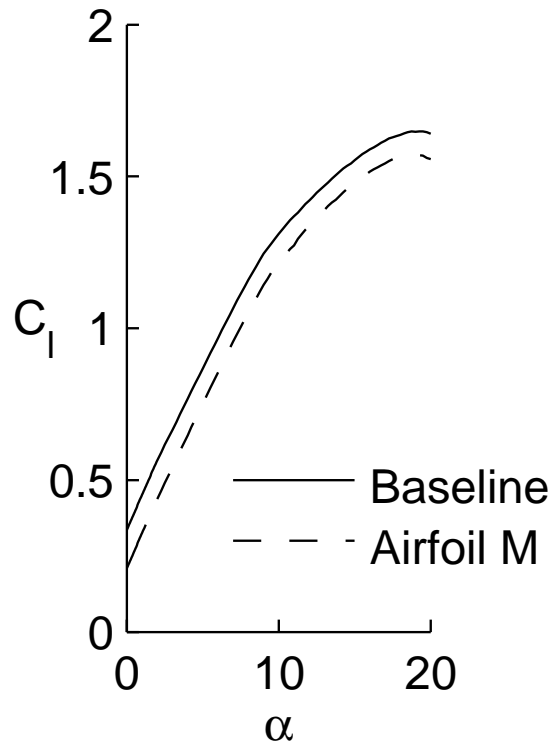


Figure 4.1: Lift curves for the Baseline airfoil and airfoil M

## 4.2.2 Extension of the Approaches for Adaptive Airfoils

It was shown in Sec. 3.4.3 that when an airfoil was tailored for both  $V_{max}$  and  $R_{max}$  the thickness of the airfoil increases as a result of the design. To counteract this, the design method can be extended to incorporate aircraft performance considerations in the design of adaptive airfoils. It is well known that the low-drag region (LDR or drag bucket) of an airfoil drag polar can be shifted by the deployment of a trailing-edge flap, also known as a cruise flap. Positive deflection of the cruise flap will cause the LDR to move to a higher  $C_l$ , whereas negative deflection will cause the LDR to move to a lower  $C_l$ .<sup>30,31</sup> This trend can be seen in Fig. 4.2. In the figure, the drag polars for the NASA NLF(1)-0215F airfoil with various flap deflections are shown along with the points corresponding to the upper and lower corners of the LDR. It can be seen that as the flap is deflected, the LDR moves to higher and lower  $C_l$  values, depending on flap deflection. The movement of the LDR occurs along a line, which can be straight or have a slight curvature depending on the airfoil. This trend was also shown to occur for changes to airfoil camber for non-flapped airfoils in Ref. 17. This “low-drag” curve is marked in Fig. 4.2 by a heavy dashed line. Because the use of a cruise flap will move the LDR along the low-drag curve, a cruise flap can be used to effectively widen the LDR of the airfoil drag polar. This widening of the LDR will help to avoid the large increase in thickness that occurs when an airfoil is tailored for both  $V_{max}$  and  $R_{max}$ . The current design method (Chapter 3) is being extended to handle the design of adaptive airfoils (with cruise flaps) while using the aircraft performance considerations in determining the ideal values for  $C_l^{low}$  with flap up and  $C_l^{up}$  with flap down.

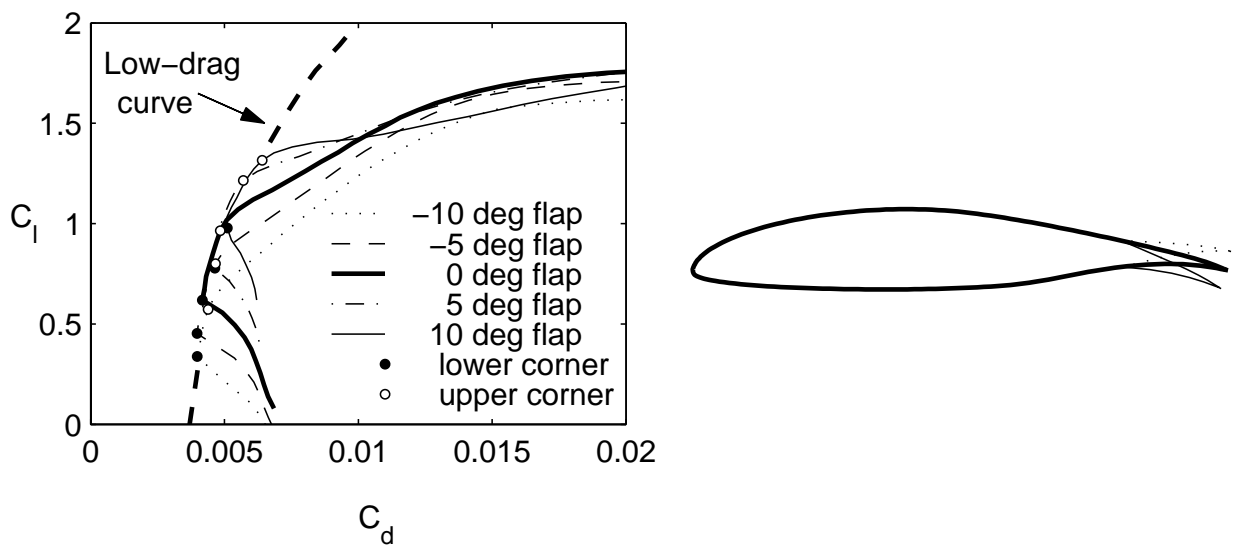


Figure 4.2: Drag polars for NASA NLF(1)-0215F airfoil with various flap deflections from XFOIL analysis

# Chapter 5

## References

- <sup>1</sup> Mangler, W., *Die Berechnung eines Tragflugelprofiles mit vorgeschriebener Druckverteilung*, Vol. 1 of *Jahrbuch der deutschen Luftfahrtforschung*, pp. 46–53, (translated as Air Ministry of London Translation No. 932, 1940).
- <sup>2</sup> Lighthill, M. J., “A New Method of Two-Dimensional Aerodynamic Design,” Aeronautical Research Council R&M 2112, April 1945.
- <sup>3</sup> Henderson, M. L., “Inverse Boundary-Layer Technique for Airfoil Design,” Vol. 1 of *Advanced Technology Airfoil Research*, NASA CP-2045, Part 1, March 1978, pp. 383–397.
- <sup>4</sup> Eppler, R., “Direkte Berechnung von Tragflugelprofilen aus der Druckverteilung,” *Ingenieur-Archive*, Vol. 25, No. 1, 1957, pp. 32–57, (translated as “Direct Calculation of Airfoil from Pressure Distribution,” NASA TT F-15, 417, 1974).
- <sup>5</sup> Eppler, R. and Somers, D. M., “A Computer Program for the Design and Analysis of Low-Speed Airfoils,” NASA TM 80210, August 1980.
- <sup>6</sup> Eppler, R., *Airfoil Design and Data*, Springer-Verlag, New York, 1990.
- <sup>7</sup> Somers, D. M., “Design and Experimental Results for a Flapped Natural-

- Laminar-Flow Airfoil for General Aviation Applications,” NASA TP 1865, June 1981.
- <sup>8</sup> Somers, D. M., “Design and Experimental Results for a Natural-Laminar-Flow Airfoil for General Aviation Applications,” NASA TP 1861, June 1981.
- <sup>9</sup> Selig, M. S., Donovan, J. F., and Fraser, D. B., *Airfoils at Low Speeds*, Soartech 8, SoarTech Publications, Virginia Beach, Virginia, 1989.
- <sup>10</sup> Selig, M. S. and Maughmer, M. D., “A Multi-Point Inverse Airfoil Design Method Based on Conformal Mapping,” *AIAA Journal*, Vol. 30, No. 5, May 1992, pp. 1162–1170.
- <sup>11</sup> Selig, M. S. and Maughmer, M. D., “Generalized Multipoint Inverse Airfoil Design,” *AIAA Journal*, Vol. 30, No. 11, November 1992, pp. 2618–2625.
- <sup>12</sup> Stevens, W. A., Goradia, S. H., and Braden, J. A., “Mathematical Model for Two-Dimensional Multi-Component Airfoils in Viscous Flows,” NASA CR 1843, July 1971.
- <sup>13</sup> Pinella, D. F. and Garrison, P., *CMARC — A Three-Dimensional Panel Code*, AeroLogic, Los Angeles, CA, 1996.
- <sup>14</sup> Gopalarathnam, A. and Selig, M. S., “Multipoint Inverse Method for Multi-element Airfoil Design,” *Journal of Aircraft*, Vol. 35, No. 3, May–June 1998, pp. 398–404.
- <sup>15</sup> Gopalarathnam, A. and Selig, M. S., “A Hybrid Approach to Inverse Design of Complex Aerodynamic Systems,” AIAA Paper 2000–0784, January 2000.
- <sup>16</sup> Gopalarathnam, A. and Selig, M. S., “Hybrid Inverse Airfoil Design Method for Complex Three-Dimensional Lifting Surfaces,” *Journal of Aircraft*, Vol. 39, No. 3, May–June 2002, pp. 409–417.

- <sup>17</sup> Gopalarathnam, A. and Selig, M. S., “Low-Speed Natural-Laminar-Flow Airfoils: Case Study in Inverse Airfoil Design,” *Journal of Aircraft*, Vol. 38, No. 1, January–February 2001, pp. 57–63.
- <sup>18</sup> Jepson, J. K. and Gopalarathnam, A., “Inverse Airfoil Design via Specification of the Boundary-Layer Transition Curve,” AIAA Paper 2003–0212, January 2003.
- <sup>19</sup> Maughmer, M. D. and Somers, D. M., “Figures of Merit for Airfoil/Aircraft Design Integration,” AIAA Paper 88–4416, September 1988.
- <sup>20</sup> Gopalarathnam, A. and McAvoy, C. W., “Effect of Airfoil Characteristics on Aircraft Performance,” *Journal of Aircraft*, Vol. 39, No. 3, 2002, pp. 427–422.
- <sup>21</sup> Selig, M. S., Gopalarathnam, A., Giguère, P., and Lyon, C. A., “Systematic Airfoil Design Studies at Low Reynolds Numbers,” *Fixed and Flapping Wing Aerodynamics for Micro Air Vehicle Applications*, edited by T. J. Mueller, Vol. 195 of *Progress in Astronautics and Aeronautics*, American Institute of Aeronautics and Astronautics, 2001, pp. 143–167.
- <sup>22</sup> Somers, D. M., “Subsonic Natural-Laminar-Flow Airfoils,” *Natural Laminar Flow and Laminar Flow Control*, edited by R. W. Barnwell and M. Y. Hussaini, Springer-Verlag, New York, 1992, pp. 143–176.
- <sup>23</sup> Drela, M., “Low Reynolds-Number Airfoil Design for the M.I.T. Daedalus Prototype: A Case Study,” *Journal of Aircraft*, Vol. 25, No. 8, August 1988, pp. 724–732.
- <sup>24</sup> Drela, M., “XFOIL: An Analysis and Design System for Low Reynolds Number Airfoils,” *Low Reynolds Number Aerodynamics*, edited by T. J. Mueller, Vol. 54

- of *Lecture Notes in Engineering*, Springer-Verlag, New York, June 1989, pp. 1–12.
- <sup>25</sup> Drela, M. and Giles, M. B., “Viscous-Inviscid Analysis of Transonic and Low Reynolds Number Airfoils,” *AIAA Journal*, Vol. 25, No. 10, October 1987, pp. 1347–1355.
- <sup>26</sup> Press, W. H., Teukolsky, S. A., Vetterling, W. T., and Flannery, B. P., *Numerical Recipes in Fortran — The Art of Scientific Computing*, Cambridge University Press, New York, 2nd ed., 1992.
- <sup>27</sup> Houghton, E. L. and Carpenter, P., *Aerodynamics for Engineering Students*, John Wiley and Sons, Inc., New York, 1993.
- <sup>28</sup> Gopalarathnam, A., Selig, M. S., and Hsu, F., “Design of High-Lift Airfoils for Low Aspect Ratio Wings with Endplates,” AIAA Paper 97–2232, June 1997.
- <sup>29</sup> Jepson, J. K. and Gopalarathnam, A., “Incorporation of Aircraft Performance Considerations in Inverse Airfoil Design,” AIAA Paper 2003–3499, June 2003.
- <sup>30</sup> McAvoy, C. W. and Gopalarathnam, A., “Automated Trailing-Edge Flap for Airfoil Drag Reduction Over a Large Lift-Coefficient Range,” AIAA Paper 2002–2927, June 2002.
- <sup>31</sup> McAvoy, C. W. and Gopalarathnam, A., “Automated Cruise Flap for Airfoil Drag Reduction Over a Large Lift Range,” *Journal of Aircraft*, Vol. 39, No. 6, November–December 2002, pp. 981–988.

# Appendix A

## Brent's Method for Root Finding

This appendix presents a brief description of Brent's method<sup>26</sup> which was used to determine the value of  $C_{ltrans}$  at a given location. The method combines super-linear convergence with bisection steps. By doing this, it can accommodate numerous types of functions using a combination of root bracketing, bisection and inverse quadratic interpolation. The method uses three points to determine the root: two for bracketing,  $(a, f(a))$  and  $(c, f(c))$ , and one for the root estimate,  $(b, f(b))$ . The estimate for the root,  $x$ , can be expressed using Eqs. A.1– A.6. If  $P/Q$  falls out of bounds, Brent's method will take a bisection step. This method is useful since it combines the reliability of bisection methods with the speed of higher order methods.

$$x = b + P/Q \tag{A.1}$$

$$P = S[T(R - T)(c - b) - (1 - R)(b - a)] \tag{A.2}$$

$$Q = (T - 1)(R - 1)(S - 1) \tag{A.3}$$

$$R = f(b)/f(c) \tag{A.4}$$

$$S = f(b)/f(a) \tag{A.5}$$

$$T = f(a)/f(c) \tag{A.6}$$

# Appendix B

## Skin-Friction Drag Estimate

This appendix briefly presents the airfoil skin-friction estimation method used to determine the drag of the airfoil. This approximation was taken from Ref. 27. Figure B.1 shows the flat-plate boundary-layer model used in the method. It is seen that a laminar boundary-layer forms at the leading edge of the plate and then transitions to turbulent further downstream. The total skin-friction over the plate can be found by adding the skin-friction for the laminar portion to the skin-friction for the turbulent portion. The amount of skin-friction due to laminar layer is the same as the skin-friction due to a turbulent layer that has the same momentum thickness at the transition location. If laminar layer momentum thickness is set equal to turbulent layer momentum thickness at this location, as shown in Eq. B.1, then the length of turbulent layer to obtain the same amount of skin-friction,  $X_{Tt}$ , can be found. The resulting expression for  $X_{Tt}$  is shown in Eq. B.2. Once  $X_{Tt}$  is determined, the total skin-friction on the flat plate can be found by calculating the skin friction for a turbulent layer of length  $L - X_t + X_{Tt}$  as shown in Eq. B.3.

$$\theta_L = 0.646X_t\left(\frac{\nu}{U_\infty X_t}\right)^{1/2} = 0.037X_{Tt}\left(\frac{\nu}{U_\infty X_{Tt}}\right)^{1/5} = \theta_T \quad (\text{B.1})$$

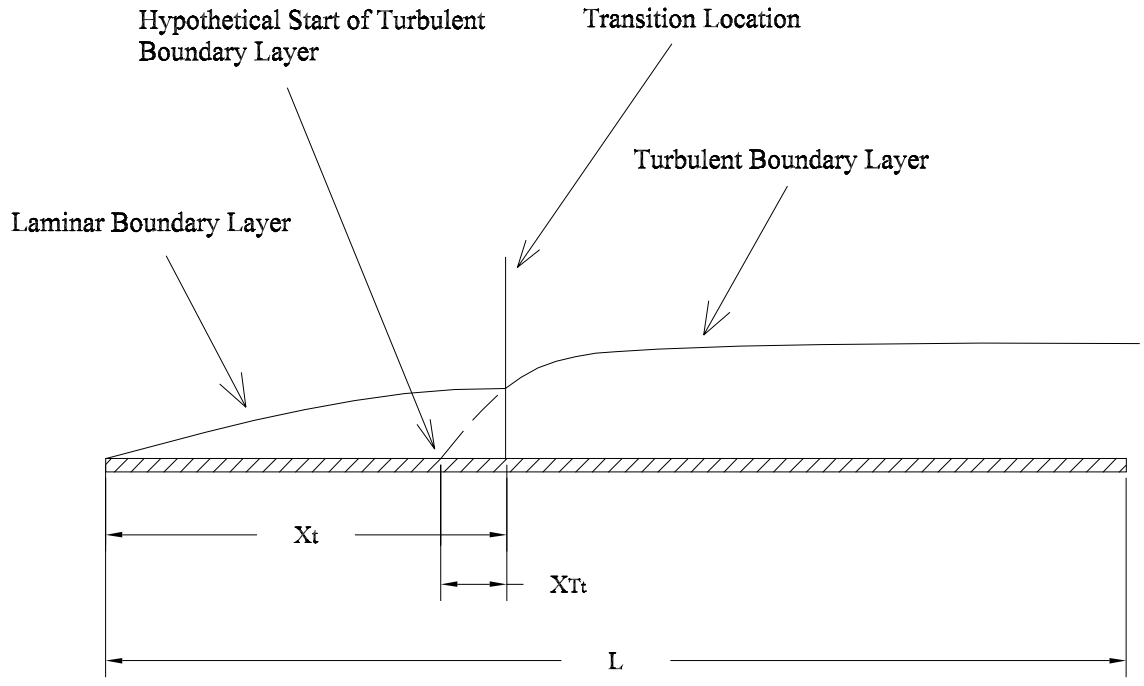


Figure B.1: Flat Plate Boundary-Layer Approximation

$$X_{Tt} = \frac{35.5X_t^{5/8}}{Re^{3/8}} \quad (B.2)$$

$$C_f = 0.0744\left(\frac{\nu}{U_\infty}\right)^{1/5} \frac{(L - X_t + X_{Tt})^{4/5}}{L} \quad (B.3)$$